VELOSTAT SENSOR ARRAY FOR OBJECT RECOGNITION AND HUMAN POSTURE RECOGNITION

by

LIANGQI YUAN

A thesis submitted in partial fulfillment of the
requirements for the degree of

ELECTRICAL AND COMPUTER ENGINEERING

2022

Oakland University
Rochester, Michigan

Thesis Advisory Committee:

Jia Li, Ph.D., Chair
Hongwei Qu, Ph.D., Co-chair
Manohar Das, Ph.D.

To my mother and father

ACKNOWLEDGMENTS

The two-year graduate education I received at Oakland University was unparalleled and rewarding. There is no doubt that I have grown into a qualified researcher in the past two years, which also laid the foundation for my future academic career.

I would like to express my utmost respect and gratitude to the mentors, professors, and peers who have given me inspiration, guidance, and assistance. First, I would like to thank Dr. Jia Li for her guidance on signal processing and machine learning and the inspiration, evaluation, and improvement for my entire project. Second, I also remain grateful to the aid of Dr. Hongwei Qu's definition, summarization, and sorting of piezoresistive sensors and material properties. Third, I would like to thank Dr. Manohar Das for his teaching, understanding, and advice. Fourth, I would like to thank my friends, classmates, and peers for their valuable suggestions and support for experiments, data collection, and analysis.

Finally, I thank my family for their understanding and support of my academic career, particularly during the most challenging period of the Covid-19 pandemic. Especially, the companionship, guardianship, and encouragement of my cat Purty over the past two years are my motivation to persevere.

Part of the results of this thesis has been published in [1][2]. This research is supported by the AFOSR grant FA9550-21-1-0224.

Liangqi Yuan

ABSTRACT

VELOSTAT SENSOR ARRAY FOR OBJECT RECOGNITION AND HUMAN POSTURE RECOGNITION

by

LIANGQI YUAN

Adviser: Professor Jia Li, Ph.D.

Pressure as one of the patterns of objects and humans has always been necessary research and has a wide range of applications in recognition and prediction. This thesis presents a cost-effective pressure sensing system for object recognition and human posture recognition. During the design process of the pressure sensing system, three different applications have been proposed: an Object Recognition Board, a Smart Cushion, and a Smart Bed Sheet, which are used to recognize ten objects, five sitting postures, and four sleeping postures, respectively. The pressure sensing system consists of a 27x27 piezoresistive sensor array made of carbon composite material Velostat, a signal processing subsystem for signal scanning, amplification, registration, and generation. A convolutional neural network is used to classify various objects through the pressure signals produced and processed by the sensing array. Based on systematic characterizations and calibrations of sensing materials and system sensitivity, three experiment setups are established. For pressure images collected with the preestablished three experiment setups, the accuracy of object recognition, sitting posture recognition, and sleeping posture recognition achieved 0.9914, 0.9660, and 0.9990, respectively.

TABLE OF CONTENTS

ACKNOWLEDGMENTS iv

ABSTRACT v

LIST OF TABLES viii

LIST OF FIGURES ix

LIST OF ABBREVIATIONS xi

CHAPTER ONE
INTRODUCTION 1

1.1 Overview 1

1.2 Properties of Velostat Materials 2

1.3 Piezoresistive Sensor Based on Velostat 4

1.4 Applications Based on Pressure Sensor Array 7

1.5 Thesis Contribution to the Current State of Knowledge 11

1.6 Thesis Outline 12

CHAPTER TWO
VELOSTAT AS PIEZORESISTIVE SENSING MATERIAL 13

2.1 Overview 13

2.2 Parameterization of Velostat Material 13

CHAPTER THREE
VELOSTAT SENSOR ARRAY 18

3.1 Overview 18

3.2 Design and Fabrication of Velostat Sensor Array 18

TABLE OF CONTENTS—Continued

3.3 Resistance Sensitivity 21

3.4 Quasi-Static Response 24

CHAPTER FOUR
APPLICATION IMPLEMENTATION AND CLASSIFICATION 32

4.1 Overview 32

4.2 Contrast Enhancement 32

4.3 Convolutional Neural Network 36

4.4 Object Recognition Board 38

4.5 Smart Cushion 44

4.6 Smart Bed Sheet 48

CHAPTER FIVE
CONCLUSION 56

5.1 Overview of Thesis 56

5.2 Future Directions 57

REFERENCES 59

LIST OF TABLES

Table 1	Parameter setting of sensor array performance measurement.	28
Table 2	Performance of four pixels analog reading G under unloading, loading, and release states.	29
Table 3	Velostat sensor array characteristic parameters.	31
Table 4	Average, variance and standard deviation of nine pixels analog reading G.	34
Table 5	Comparison of accuracy between ResNet-PI and four other classification algorithms.	43
Table 6	The specific characteristics of the proposed Object Recognition Board, Smart Cushion, and Smart Bed Sheet.	55

LIST OF FIGURES

Figure 1	SEM image of Velostat material at 5000 times magnification, (a) without pressure, (b) with pressure.	14
Figure 2	Velostat cross-sectional schematic diagram, (a) normal state, (b) with pressure, (c) tension applied, (d) mechanical bending.	15
Figure 3	Evaluation method of Velostat resistance sensitivity, (a) Push Pull Force Gauge, (b) measuring circuit.	16
Figure 4	Schematic circuit diagram of the sensor array.	19
Figure 5	Schematic diagram of the sensor array.	20
Figure 6	PCB for signal processing subcircuits.	21
Figure 7	Resistance vs. pressure curve.	22
Figure 8	Schematic diagram of the analog reading G curve with time.	25
Figure 9	Analog reading G change curve of four pixels in three states.	28
Figure 10	ResNet-PI architecture block diagram.	37
Figure 11	Schematic diagram of the Object Recognition Board.	38
Figure 12	Object Recognition Board.	39
Figure 13	Ten objects were used to collect object pressure information. The order from left to right and top to bottom is Pepsi, Perrier, one, two, iron block, seven, three, five, nine, eight. Since four, six, and nine are easily confused, only one of them is selected. Pepsi, Perrier, and iron block collect the bottom pressure image in the direction shown in the figure. Seven LEGO numbers are flipped to collect pressure images of the numbers side.	40
Figure 14	Resistance vs. pressure curve. (a) Actual resistance and effective resistance comparison, the two exponential curves fitting of the actual resistance, and the actual resistance intersection point is 65 Newtons. (b) Effective resistance with pressure curve, the two exponential curves fitting of the effective resistance, the effective resistance intersection point is 55 Newtons.	41

Figure 15	Confusion matrix for ResNet-PI recognizing ten objects.	42
Figure 16	ResNet-PI training model for 10 objects, (a) model accuracy curve, (b) model loss curve.	43
Figure 17	Human sitting posture collection system. (a) Overall sitting posture collection system includes the Smart Cushion, signal processing subsystem PCB and a host computer, (b) the Smart Cushion fixed on the laboratory chair seat, (c) the signal processing subsystem PCB fixed behind the laboratory chair backrest, (d) schematic diagram of the Smart Cushion structure.	45
Figure 18	Schematic diagram of 5 sitting postures in human daily activities, (a) normal, (b) forward, (c) backward, (d) left & right, (e) upright.	46
Figure 19	The pressure image of the subject's "normal" sitting posture after contrast enhancement, filtering, and resizing.	47
Figure 20	Confusion matrix of sitting posture recognition, (a) test dataset, (b) second validation dataset.	49
Figure 21	Schematic diagram of the Smart Bed Sheet, (a) structure, size, and actual sensing area, (b) separated sensor elements size and spacing.	51
Figure 22	Actual image of the Smart Bed Sheet.	52
Figure 23	Schematic diagram of four sleeping postures, (a) supine, (b) prone, (c) left lateral, (d) right lateral.	52
Figure 24	The pressure image of the subject's "supine" sleeping posture after contrast enhancement, filtering, and resizing.	53
Figure 25	Confusion matrix of sleeping posture recognition, (a) test dataset, (b) second validation dataset.	54

LIST OF ABBREVIATIONS

CNN	Convolutional Neural Network
IMU	Inertial Measurement Unit
SNR	Signal-to-Noise Ratio
CRNN	Convolutional Recurrent Neural Network
CDNN	Convolutional Dense Neural Network
SEM	Scanning Electron Microscope
SISO	Single-Input Single-Output
PCB	Printed Circuit Board
ResNet-PI	ResNet for Pressure Image
Conv	2D Convolution Filter
ReLU	Rectified Linear Unit
BaN	Batch Normalization
Avg Pool	Average Pooling
PVC	Polyvinyl Chloride
LSTM	Long short-term memory

CHAPTER ONE

INTRODUCTION

1.1 Overview

Tactile sensing is one of the most fundamental sensing mechanisms the human body develops. In the current world of human-computer interaction and intelligent health, the tactile signal has been widely used as inputs for information processing and control, enabling machine recognition of external excitations. The current areas where such recognition and interaction are enthusiastically pursued include, but are not limited to, medical treatments [3][4], biological products [5][6], wearable electronics [7][8], and robotics [9][10]. In a tactile sensing system, an electrical signal is generated as a response to physical parameters such as temperature, pressure, vibration, texture, friction, etc. when the object is in close contact with the tactile sensor [3][11]. Pressure sensor is one of the largest categories of all sensors thanks to its diverse sensing mechanisms and, more importantly, easy device fabrication process, thus possible low cost. Moreover, due to the miniature size enabled by semiconductor process-based microfabrication technologies, a variety of pressure sensors have been adopted in wearable electronics and medical devices where flexible sensor deployment is crucial.

Based on their physical responses and sensing mechanisms, pressure sensors can mainly be categorized into the following types, i.e., capacitive, piezoelectric, optical, and piezoresistive [11][12][13][14]. Capacitive pressure sensors feature high sensitivity, low-temperature dependence, and low noise floor, which are desirable for applications with high precision and harsh environments [15][16][17]. Piezoelectric materials have found promising applications in wearable electronics thanks to their dual energy flow – can be used as both sensing and energy generating elements. In this area, a variety of triboelectric devices with self-powering capability have been actively attempted, despite that the fabrication processes for such materials and devices are normally not compatible with standard technologies [12]. Optical pressure sensors have great attributes such as high sensitivity and outstanding interference immunities. However, their bulky system configurations hinder their applications in many areas where deployment flexibility is a concern [18][19]. Piezoresistive pressure sensors, however, take many forms of materials and structures for a large array of applications. Because of their overall easy fabrication, low-cost, simple signal processing circuitry, and standard data acquisition process, piezoresistive sensors have steadily been the dominating category in pressure sensing [20][21]. In contrary to silicon and metal-based piezoresistive sensors and strain gains for process control and specific pressure monitoring, some flexible piezoresistive materials have demonstrated their great advantages in easy deployment, which is of particular importance for biomedical and human-machine interacting systems.

This chapter introduces the properties of the carbon composite material Velostat, the Velostat-based piezoresistive sensor and its shortcomings, related applications, and existing technologies. The contributions and outline of this thesis are presented at the end of this chapter.

1.2 Properties of Velostat Materials

The past research on Velostat has been focused on characterizations of the electrical and mechanical properties associated with particular applications of the material. In [30] and [55], piezoresistive sensitivity, hysteresis, repeatability, etc. have been investigated. Some researchers have confirmed the usability of the material in terms of hysteresis and repeatability. In addition, other papers do not have a unified measurement unit (Newtons; Pascals) [56]. Our research found that the use of Pascals is an inappropriate measurement unit for the Velostat sensor. It's well known that various parameters related to the deployment of Velostat material as a sensing element are involved when such a sensing system is constructed. For instance, when used as a force sensor where Velostat material is made contact with certain electrodes as a measuring instrument, the changes of the Velostat sensor resistance are a function of the following factors: Velostat material properties, applied force, and applied time, the contact area between the measuring instrument and the Velostat sensor, the area of the intersection of the conductive wire, and the relative position of the center of the measuring instrument, and the intersection of the conductive wire, etc. However, thus far, not too much research has been conducted on the relations between the resistance of the Velostat sensor and the applied pressure and applied time from the application perspective of object recognition. In our research using the Velostat sensor as the piezoresistor, the relative position of the element and the force measuring instrument is relatively static - the probe of the force measuring instrument is always located in the center of the measuring element, which allows us to maintain other conditions unchanged to characterize the pressure response of the sensing element. Based on our systematic studies on the piezoresistive responses of Velostat, including the sensitivity and resistance changes under different pressures and times, we have proposed appropriate experiment setups with specific object weight to obtain higher recognition accuracy.

In designing the above particular experiment setups for our purpose, we have addressed some practical issues in previously reported applications of Velostat sensors. Dzedzickis et al. [56] reported the effects of surface roughness of new and used Velostat materials, as well as the loading, on the stability of sensor responses. Other researchers [28][57] have investigated the overall time dependence of the output voltage of the Velostat sensors. However, none of the above research has drawn a conclusion as to when data acquisition should be performed after the force or pressure is applied to the sensor for reliable image construction.

This happens to be one of the most critical influencing parameters in the establishment of a pressure image database. On the one hand, if the collection time is too short, a large amount of pressure image information under different conditions will be lost. On the other hand, if the collection time is too long, redundancy occurs with a large number of duplicated data in the dataset, which will reduce the processing resources. We investigated this issue by characterizing the data acquisition system of the Velostat sensor array by examining the transient response of the sensor resistance systematically. Comprehensive studies on steady-state values, variance, rise, fall, and settling transients in unloaded, loaded, and released states of the sensor array resistance are conducted to find the optimal responses of the sensor array. An experiment setup and measurement scheme for optimization of data collection and release time has been established to ensure the diversity, richness, and universality of pressure image data sets.

1.3 Piezoresistive Sensor Based on Velostat

To this end, various pressure sensor arrays based on Velostat, an elastic polymer with conductive additive with piezoresistive characteristics, have been extensively explored recently [22][23]. Sundaram et al. [24] have demonstrated tactile gloves for object-grasping robotics, in which a convolutional neural network (CNN) is employed to recognize the type of objects and judge the responding gestures of the robotics through the signals provided by Velostat sensors integrated into the gloves. Chen et al. [25][26] have developed pressure sensor insoles to assist inertial measurement unit (IMU) for indoor human positioning. Hudec et al. [27] have utilized Velostat pressure sensors in their mattress designed to detect the position of a lying person to prevent bedsores. Hopkins et al. [28] used a Velostat strip pressure sensor to characterize the lower limb pressure in adaptive tests in a prosthesis. Niu et al. [29] evaluated athletic helmet's comfort and stability level based on the data acquired from a flexible pressure sensor array in the helmet. In the above emerging areas as customized and remote healthcare, tele-sportscare, etc., Velostat pressure sensors have been playing an increasingly important role in providing original signals for subject monitoring.

However, compared with rigid piezoresistive sensors made of crystals such as silicon and metals, Velostat pressure sensors commonly suffer a certain extent of performance disadvantages such as inferior repeatability, hysteresis, and nonlinearity, which originate from some notorious defects of such polymeric material, including a certain degree of plastic deformation, non-uniformity in material composite and texture [30]. Moreover, when used in sensor arrays, due to the plastic characteristic of Velostat and the chaotic currents in the resistor array, considerable crosstalk in neighboring grids has been consistently observed [31]. Furthermore, the non-uniformity in material composite and texture have also contributed to even the non-uniformity in the crosstalk.

Velostat material can be thought of as a piezoresistive resistor, and this resistive sensor array usually suffers from various electrical disturbances that degrade the accuracy, reliability, and robustness of the system. The crosstalk is a critical issue that affects image recognition accuracy. It originates from both mechanical and electrical responses of the sensor. Mechanical crosstalk is caused by the non-ideal force diffusion of the flexible material under pressure [58]. Considering the fabrication of sensor arrays, we only utilize separated sensors in the Smart Bed Sheet to limit the effects of mechanical crosstalk. Electrical crosstalk is a widespread problem in resistive sensor arrays, which usually causes loss of accuracy [59][60][61] and ghosting [62]. The electrical crosstalk can be divided into two types, i.e., electrical crosstalk Type A and Type B. The Type A crosstalk is caused by the random current flowing through the Velostat resistance in related areas in the sensor or sensor array. Particularly, for the sensor structure used in this thesis, this type of crosstalk is related to the surface resistance of the Velostat material. Based on the observation that compared with the bulk cross-sectional resistance that is employed for pressure sensing, the resistivity of the surface layer is relatively low in the thickness direction (< 31,000 ohms/sq.cm), the sensing error caused by this resistance element is relatively small thus can be neglected. Detailed studies on the effect of such surface resistance will be reported in the future. Electrical crosstalk type B is due to the fact that current always flows through a path with smaller resistance, which is a critical element in the determination of the performance of the sensor in this study. The proposed experimental setup aims at addressing this crosstalk particularly. The cause of the specific Type B electrical crosstalk is that when calculating the resistance of a target piezoresistive sensor element (cross spot), not only the current flows through this target piezoresistive sensor, but also through the adjacent sensors. It's equivalent to a parallel connection of several piezoresistive sensors. Many researchers have proposed many solutions [63][64] in this regard. Hidalgo-López et al. [31] add additional calibration rows and columns to the original resistance array. Suprapto et al. [65] used diodes to shield the reverse current of each sensor. Yet, most of the methods are inadequate in ensuring the needed flexibility and signal-to-noise ratio (SNR) of resistor arrays. To address this challenge, we choose a "zero potential method" in which operational amplifiers are used as auxiliary circuits for SNR boost. Consequently, in addition to enhancing the contrast of pressure images in visualization applications, the ability of convolutional neural networks to automatically perform feature extraction on pressure images also ensures the accuracy of the system.

The above common issues with Velostat sensors would be challenging for conventional signal compensation methods. Fortunately, recent advancements in information fusion and processing have opened a new window in signal processing and enhancement [32]. Particularly, powerful artificial intelligence has found their applications in addressing the otherwise tenacious problems as in the Velostat pressure sensors and arrays.

1.4 Applications Based on Pressure Sensor Array

In recent years, with the continuous development in the fields of robotics, human-computer interaction, and intelligent life, achieving high-precision object recognition and human gesture recognition is a challenge. Object recognition technology is widely used in robots to assist robotic arm in grabbing objects by obtaining information such as the shape, position, and angle of the object. For object recognition, computer vision provides a feasible solution. However, computer vision has limitations in handling details such as object mass, roughness, and stiffness. For example, computer vision has difficulty distinguishing objects of similar shapes, such as real fruits and fruit models. Therefore, the tactile sensing system is a significant supplement for object recognition because it is able to capture the details of multiple attributes of the object and is a low-cost solution.

The monitoring and recognition of human sitting and sleeping postures are important ways to improve people's life smart, automation, and health. Accurate and robust sitting posture recognition is an important technique to provide smart life for sedentary people, such as the elderly, students, and drivers. Sitting posture recognition can effectively prevent diseases [33][34], correct sitting posture [35][36], and improve driving safety [37][38]. Similar to sitting posture, human sleeping posture is also related to human health. Unhealthy postures also increase the dedication of people to worsening illnesses [39][40][41]. For the task of human sitting and sleeping posture recognition, researchers have proposed different solutions such as computer vision [42][43], wearable sensors [44][45], and pressure sensors [46][47][48][49]. For human applications such as human-computer interaction, computer vision has privacy concerns for human classification tasks due to its intrusive design. Besides, the use of wearable sensors for human gesture recognition and gait analysis is also one of the popular solutions in recent years. However, wearable sensors are not suitable for daily environments due to their troublesome and uncomfortable features, especially in the elderly-led demand. Sheet with pressure sensor does not have the above problems and has a variety of solutions, which has attracted intensive research interests. Different human behaviors can produce different sitting and sleeping postures, resulting in different pressure distributions on the pressure sensor. Compared with separated pressure sensor in other literatures, the proposed pressure sensor array can be spread all over the sheet to collect complete human body pressure distribution information, which is proven to have higher accuracy, visual solutions, and is capable of handling complex tasks [50][51][52][53][54].

In addition to the physical sensing element, image processing is also essential for the force and pressure image system demonstrated in this work. Using CNN to recognize and classify tactile images has proven to be an effective method [66][67][68]. Gandarias et al. [69] developed an adaptive gripper based on the Tekscan pressure sensor array to recognize fifteen objects, including the inert objects and human limbs. This kind of gripper with pressure sensor has broad application prospects in the method of obtaining external information and the ability of external control on robotics. Compared to the commercial pressure sensor array Tekscan, the fabricated Velostat sensor array has advantages in price, flexibility, and foldability. Moreover, due to the marginal effect, the high-resolution pressure sensor array has a more expensive manufacturing cost, but the improvement in accuracy is limited. Wan et al. [70] report a sitting pressure image acquisition system to recognize sitting posture and locate the hip position, providing visualization options. However, beyond the rigid bottom required for their sensor, which can be seen that the sensor hardware of their system has the possibility of further optimization. Also, the accuracy of classifying the sitting model was lower than expected. Hu et al. [54] established a sleeping posture recognition system based on Velostat, which is similar to our methodology. However, their understanding of electrical disturbances in sensor arrays such as crosstalk is slightly weaker. In particular, the machine learning models in these literatures do not perform as well as expected when dealing with pressure images with extensive crosstalk effects. A common approach in the above literatures is to employ transfer learning on some popular neural networks. However, how to find a dataset of similar type, size, resolution, and classification tasks to pressure images is the most crucial criterion. Otherwise, it will lead to negative transfer. In this thesis, we designed our own CNN ResNet-PI suitable for pressure images, which is a lightweight neural network that requires low data volume, occupies fewer resources, and can obtain comparable accuracy.

For real-world tactile perception applications such as identification and analysis of grasping, sitting, gait, etc., classification tasks are dynamic and continuous [77][78][79][80][81]. Although it could be extended to series image data sets processing, the purpose of this thesis is to develop solutions based on the particular characteristics of the Velostat pressure sensor array we have demonstrated and some corresponding applications. Although Convolutional Recurrent Neural Networks (CRNNs), Convolutional Dense Neural Networks (CDNNs), and 3D CNNs have been tried for dynamic pressure image solutions, their performance is insufficient. The first reason is that dynamic pressure images treat multiple images as one sample, which reduces the number of samples in the pressure image dataset. The second is that complex and heavyweight neural networks such as CRNN, CDNN, and 3D CNN have more parameters, which leads to the training of the model consuming more resources. The Velostat sensor array combined with the CNN framework provides a feasible solution and mechanism for future enhancement and applications.

In our design, the pressure images generated by the Object Recognition Board, Smart Cushion, and Smart Bed Sheet have the exact resolution, so the same CNN architecture is used to train the three pressure image datasets, respectively. According to the size and resolution of the pressure images, ResNet-PI, a modified version based on ResNet18, has been demonstrated in this thesis to recognize objects, sitting posture, and sleeping posture.

1.5 Thesis Contribution to the Current State of Knowledge

In the work reported in this thesis, a 27x27 Velostat piezoresistive sensor array for objects, sitting postures, and sleeping postures recognition through pressure pattern identification is demonstrated. Three experiment setups are first developed to ensure the accuracy, reliability, and consistency of the signal generation, data rendering, and interpretation. Through the following experiments with the setups on systematic material characterizations and sensor calibrations, a baseline tactile signal database is established. Using ResNet-PI, a high-precision recognition CNN, the aforementioned system issues associated with material properties of Velostat, have been effectively tackled. The contributions of this paper are:

1. Systematic material study on the polymer composite in Velostat to understand the electrical and mechanical characteristics of the conductive material. The resistivity of the material as a function of applied pressure is studied, and the quasi-static response is also characterized.

2. Pressure sensor array design and establishment of three experiment setups and data processing scheme for quantitative evaluation of the performance of the Velostat sensor array using both electronic signals and imaging processing. The first setup is to establish a baseline for the optimized response of the system, in which a series of objects with the same weight but various shapes are used for pattern identification. In the second and third

setup, quasi-static responses of the system are characterized, with rise, fall, and settling transients being studied, respectively.

3. Based on the mechanism of the Velostat pressure sensing system and three experimental setups, we developed three applications: Object Recognition Board, Smart Cushion, and Smart Bed Sheet. In the above implementation, ResNet-PI, a residual convolutional neural network, was employed for pressure image recognition. Accuracy of 0.9914, 0.9660, and 0.9990 was observed on pressure image datasets of ten objects, five sitting postures, and four sleeping postures, respectively.

1.6 Thesis Outline

The remaining chapters of this thesis are presented as follows. Chapter Two parameterizes the properties of Velostat as a piezoresistive sensing material. Chapter Three presents the construction of signal processing circuits, fabrication and properties of Velostat sensor array, and the related experimental results, including resistance sensitivity and quasi-static response. Chapter Four demonstrated the contrast enhancement, the proposed convolutional neural network architecture, and the fabrication and classification results of three applications of the Object Recognition Board, Smart Cushion, and Smart Bed Sheet. Chapter Five summarizes the research, discussions, and future research plans.

CHAPTER TWO

VELOSTAT AS PIEZORESISTIVE SENSING MATERIAL

2.1 Overview

Although Velostat as a carbon composite material is popular in piezoresistive sensing in previous literature, the properties of Velostat materials have not been discussed. In this chapter, we systematically studied Velostat as a piezoresistive sensing material, discussed the factors affecting the resistance of Velostat, and parameterized the resistance of the Velostat material.

2.2 Parameterization of Velostat Material

Velostat material is flexible, stretchable, light, thin (0.1mm thick), and low in price. Eleven square inches of Velostat material sells for $4.95. As a polymer composite material, Velostat consists of carbon-impregnated polyethylene, a resistive material based on quantum tunneling and percolation [56][71]. Through scanning electron microscope (SEM), the changes of carbon particles (white area) and gap (black area) under pressure can be observed, as shown in Figure 1 is the surface of Velostat with a magnification of 5000x. When no pressure is applied, the gaps between the polymer clusters measure an average value of 1 micron. Under pressure, the gap is statistically reduced to approximately 0.6 microns. When pressure is applied, the gap becomes smaller, and the effective distance between the conductive elements decreases, thus the overall conductivity of the material increases.

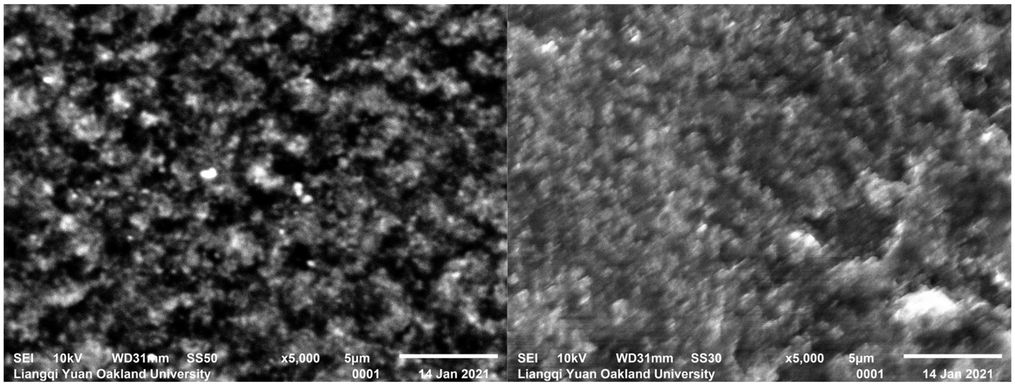

(a) (b)

Figure 1. SEM image of Velostat material at 5000 times magnification, (a) without pressure, (b) with pressure.

According to the model for conductive polymer composite materials established by Zhang et al. [72], the relative resistance of the composite material at any applied time t of pressure can be expressed as:

$$\frac{R(t)}{R_0} = f(\sigma, D, \theta, \varphi, \varepsilon_0, \psi, n) \tag{3.1}$$

where $R(t)$ is the instantaneous resistance of the composite material at applied time t; R_0 is the original resistance, σ is the applied pressure, D is the nominal diameter of the filler particles, θ is the filler volume fraction, φ is the potential barrier height, ε_0 is the original strain, ψ and n are constants related to creep behaviors in the material. When these factors are fixed, the relative resistance is only related to t, and the relative resistance decreases as t increases [72]. In our experiment, the applied pressure σ which as the object weight also needs to be taken into consideration. We fix other factors unchanged and consider σ and t as independent variables separately. At the same time, the resistance of the polymer composite material R rather than the relative resistance is studied as a dependent variable. Equation (3.1) can be rewritten as:

$$R(\sigma; t) = f(\sigma; t | D, \theta, \varphi, \varepsilon_0, \psi, n) \quad (3.2)$$

Velostat is used as the piezoresistive resistor in our sensor array design. Except for pressure, there are similarities such as tension and mechanical bending will also decrease the resistivity of Velostat. Figure 2 shows a schematic diagram of the changes in the gap (black area) and conductive carbon particles (white dot) inside the Velostat when pressure, tension, and mechanical bending are applied to Velostat.

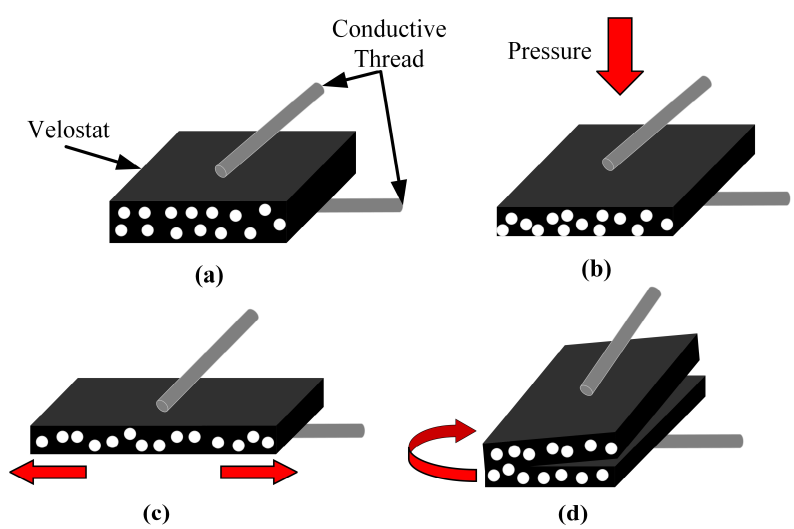

Figure 2. Velostat cross-sectional schematic diagram, (a) normal state, (b) with pressure, (c) tension applied, (d) mechanical bending.

In order to test the influence of the applied pressure σ and applied time t on the Velostat resistance, a setup with a push-pull force gauge (Max Load 500 N Stand Tester) was designed in this research, as shown in Figure 3 (a). The setup features a single-input single-output (SISO) characterization scheme, as illustrated in Figure 3 (b).

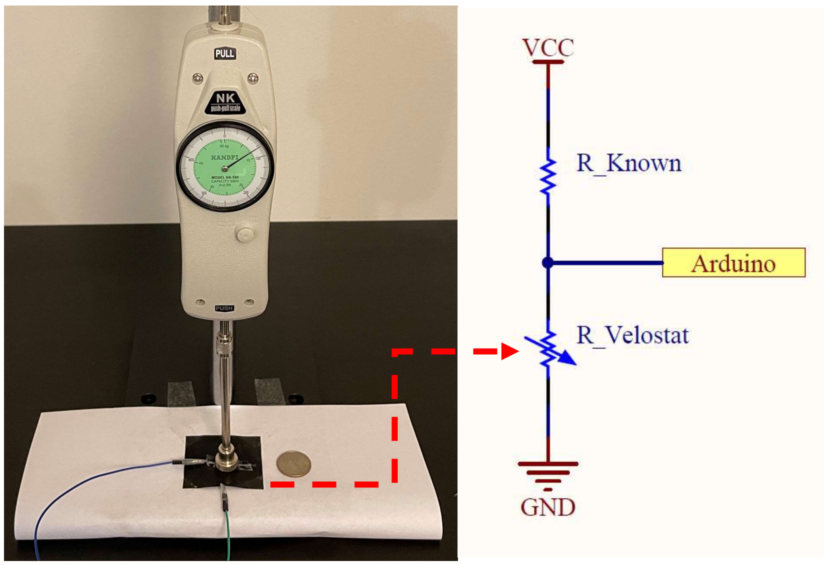

(a) (b)

Figure 3. Evaluation method of Velostat resistance sensitivity, (a) Push Pull Force Gauge, (b) measuring circuit.

The resistance of Velostat was calculated using Arduino Uno and breadboard. Figure 3 (b) shows the schematic diagram of the circuit. The basic principle is a voltage divider circuit. The resistance value of Velostat can be calculated by:

$$\mathrm{R}_{Velostat} = \mathrm{R}_{Known} \frac{V_{out}}{V_{cc} - V_{out}} \tag{3.3}$$

where $\mathrm{R}_{Velostat}$ is the resistance value of Velostat, R_{Known} is the known resistance value, V_{out} is the output voltage, which is the voltage converted from the value read by the

Arduino analog pin, and V_{cc} is the power supply voltage. Push-Pull Force Gauge is used to apply different pressures and different times, and the results are presented in Chapter Three.

CHAPTER THREE

VELOSTAT SENSOR ARRAY

3.1 Overview

After the properties of the Velostat material are parameterized in Chapter Two, Chapter Three presents the design, fabrication, and properties experiments of the Velostat sensor array. The resistance sensitivity of the Velostat is significantly reduced due to the effect of crosstalk in the piezoresistive sensor array. We are concerned with the Velostat sensor array under the influence of crosstalk and when the idea pressure and transient response are achieved. Therefore, we designed experiments for Velostat resistance sensitivity and quasi-static response and proposed three experimental setups accordingly.

To obtain a high-quality pressure image data set, it was necessary to test the electrical properties and the effect of crosstalk on the sensor array. Using the Object Recognition Board as an example, we conducted experiments on two crucial parameters, object pressure σ and applied time t that affect the resistance of Velostat. For σ, the resistance sensitivity of the SISO sensor and a single element in the sensor array were measured respectively, and the ideal object weight was found. For t, the sensor array quasi-static response was measured, and the appropriate collection time and release time were found. These three experimental setups were used in data collection to obtain higher-quality raw pressure image datasets.

3.2 Design and Fabrication of Velostat Sensor Array

The three applications: Object Recognition Board, Smart Cushion, and Smart Bed Sheet all use the same sensor array fabrication structure and signal processing subsystem.

They only differ in protective layer material, size, and resolution. In order to use the piezoresistive material Velostat to obtain the pressure information of the object. We have fabricated a pressure sensor array with 27 rows and 27 columns. A total of 729 sensors are composed of piezoresistive resistance Velostat. We chose the zero-potential method [63][73] based on electrical grounding. This method does not require the insertion of diodes or crystals to affect the sensor array's flexibility, and the impact on SNR is minimal. Furthermore, use shift registers and analog multiplexers to scan the entire sensor array row by row to obtain each sensor array point's value. Each element in the sensor array is a pixel on the generated pressure image. Figure 4 shows the circuit structure of this method.

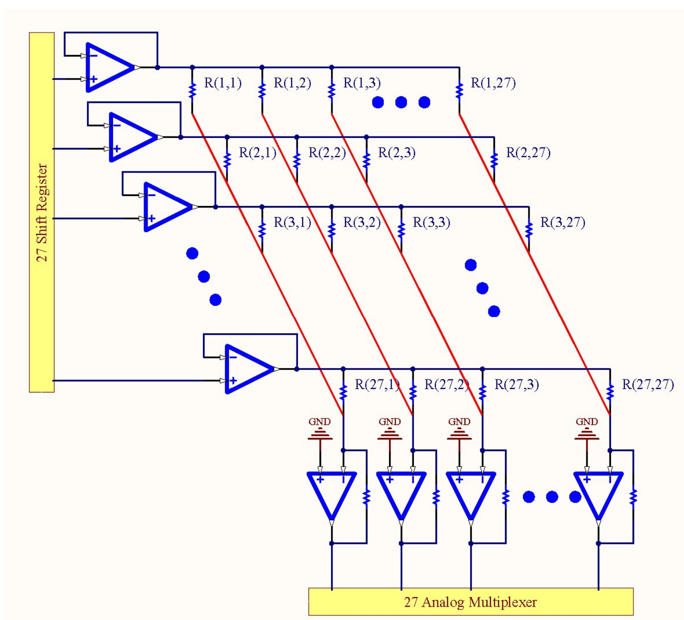

Figure 4. Schematic circuit diagram of the sensor array. Twenty-seven shift registers (four chips) and twenty-seven analog multiplexes (four chips) are used to select the rows and columns to be read. Each row and column have a grounded operational amplifier to reduce the impact of crosstalk.

As noted in Figure 4, $R(i, j)$ is the sensor element in the i-th row and j-th column of the piezoresistive resistance sensor array made by Velostat. Velostat sensor array has a seven-layer structure, and it is a symmetrical structure. The top and seventh layers are protective layers. Three applications used different protective layer materials. The second and sixth layers are adhesion layers, using 0.236mm 200MP adhesive transfer tape acrylic to ensure the firmness of the protective layer and the relative position of the conductive thread and Velostat. The third and fifth layers are the column conductive and row conductive layers, using conductive threads made of stainless-steel fibers, which are soft, easy to fabricate, and have low resistivity. The fourth layer is Velostat material. The structure diagram of the sensor array is shown in Figure 5.

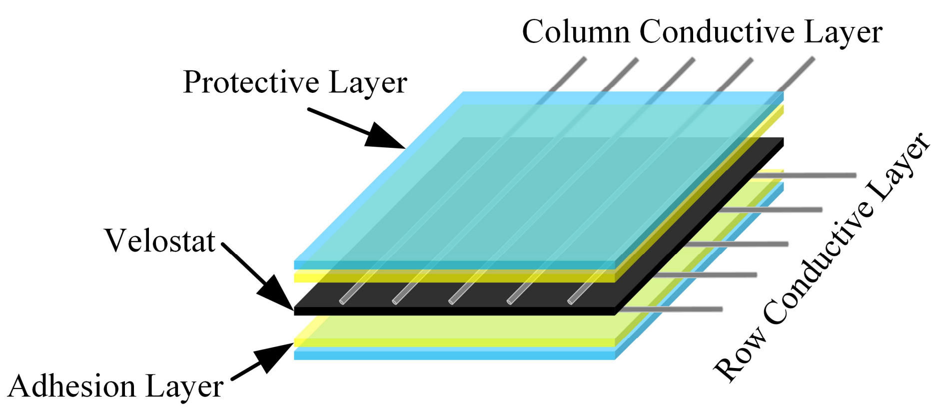

Figure 5. Schematic diagram of the sensor array. Blue is the protective layer, yellow is the adhesion layer, the silver thread is the conductive thread, and the black is Velostat.

The remaining signal processing circuit consists of operational amplifiers, shift registers, analog multiplexers, and Arduino Nano. Arduino Nano scans each element's value by switching rows and columns, and after digital signal processing, it sends each element's value to Processing to generate a pressure image. Figure 6 shows the printed circuit board (PCB) of the signal processing circuit. The DuPont line is used as the connecting line to facilitate the second production in the later stage.

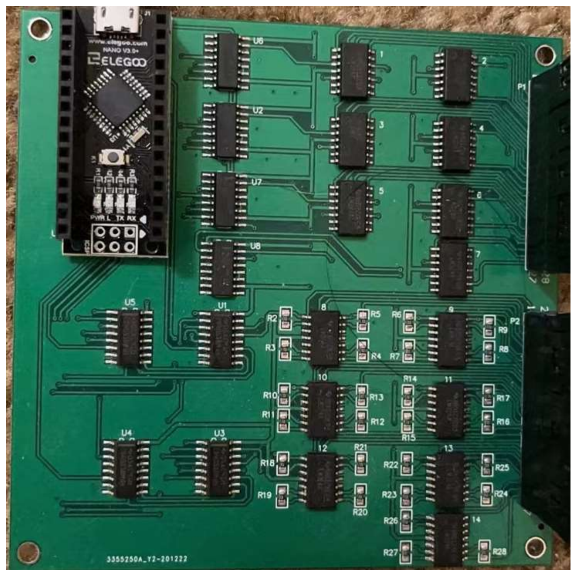

Figure 6. PCB for signal processing subcircuits.

3.3 Resistance Sensitivity

For the research of resistance sensitivity, the influence of applied time t should be eliminated as much as possible. The recording time is fixed to be a one-second delay after the pressure is applied. To reduce the jitter and the inaccuracy of delay recording, the experiment was repeated three times, and the measurements were averaged. Moreover, there was an interval of 1 hour between each experiment to restore Velostat to its initial state.

Since the resistance sensitivity of the sensor array is a direct factor in generating the pressure image, a single element in the sensor array is more worthy of attention. The resistance of a single element on the sensor array will be affected by crosstalk, and its resistance will be significantly reduced. We define the resistance of a single element in the sensor array as the effective resistance, and the resistance of the SISO sensor that is not affected by crosstalk as the actual resistance. The actual resistance and the effective resistance are compared to observe the effect of crosstalk on the sensor array. Using the circuit shown in Figure 7 and (3.3), pressure is applied to Velostat sensor cyclically to obtain the relation of the actual resistance and the effective resistance versus applied pressure σ.

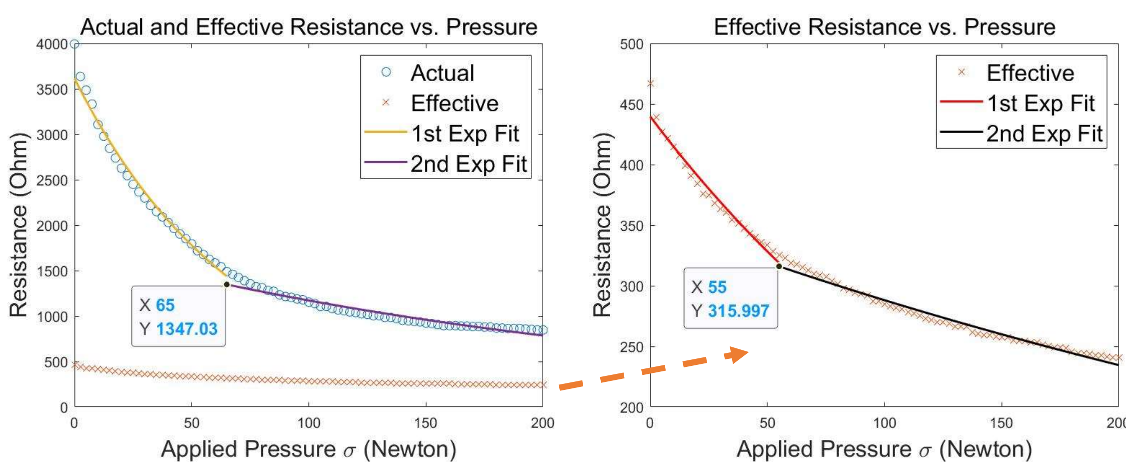

(a) (b)

Figure 7. Resistance vs. pressure curve. (a) Actual resistance and effective resistance comparison, the two exponential curves fitting of the actual resistance, and the actual resistance intersection point is 65 Newtons. (b) Effective resistance with pressure curve, the two exponential curves fitting of the effective resistance, the effective resistance intersection point is 55 Newtons.

Figure 7 (a) shows that as σ increases, the actual resistance decreases exponentially in two exponential curves, the first curve will be faster, and the second curve will be slower. The actual resistance intersection of these two exponential curves is 65 Newtons, which means that the actual resistance of the Velostat sensor is more sensitive to pressures less than 65 Newtons. At the same time, under the same pressure, the effective resistance is almost equal to one-tenth of the actual resistance.

Figure 7 (b) shows the same properties of effective resistance. When σ increases, the effective resistance decreases exponentially in two exponential curves. The intersection is 55 Newtons. According to these two intersections, the ideal weight of the object is around 60 Newtons. If the object is too light to be recognizable, additional weight (up to 60 Newtons) needs to be applied to make sensor array resistance fall to a recognizable value. This leads to the first experiment setup.

Experiment Setup 1: Object Weight. *The ideal object weight is around 60 Newtons for high accuracy.*

It is worth noting that although in our experiments, the characteristic of the faster exponential curve is not used as one of the experimental setups, it is a versatile characteristic that deserves attention. Although the selected ten rigid and easily distinguishable objects will bring higher accuracy, the pressure of the objects is evenly distributed on several elements due to their uniform texture. If due to uneven texture or objective pressure distribution, this may bring more achievable functions to the Velostat sensor array, which will be one of the future works.

3.4 Quasi-Static Response

Each element of the Velostat sensor array corresponds to each pixel on the pressure image. Due to the non-necessity and inaccuracy of the secondary resistance calculation, here we directly use the reading of the Arduino Nano as the value of the pixel, which is called the analog reading G. For applied pressure σ and applied time t that affect the Velostat sensor array resistance in (3.2), it is more appropriate to study the relationship between σ and resistance, and the relationship between t and G. Since the Velostat sensor array resistance has a higher dynamic range than G, the curve of σ and resistance can more realistically reflect the changing trend. Applied time t as a key factor of generating pressure images, directly affects the diversity and quantity of pressure image data sets, so the curve of t and G is more suitable for discussion.

Quasi-static response is defined to express the relationship between t and the analog reading G. According to our experience, during the process of applying pressure to the Velostat, the increase rate in the analog reading G will slow down. After a long enough time, G will reach a steady state. First, we define the steady-state analog reading G values in three states:

$$\overline{G_{state}} = \frac{1}{\tau}\left(\sum_{i=T_{state}-\tau+1}^{T_{state}} G_{state}(i)\right)$$
$$\text{for } state \in \{unl, load, rel\} \tag{3.4}$$

where $state$ represents three possible states. G_{unl} represents the analog reading in the unloaded state, G_{load} represents the analog reading in the loading state and G_{rel} represents the analog reading in the release state. T_{state} represents the total time of a single $state$ continuously collected, for each state we use the same formula, but T_{state} is different for each state. $G_{state}(i)$ represents the i-th G value in the continuously collected element analog reading G. Due to electrical noise and disturbance, G is in an oscillating state.

The steady-state value is obtained by averaging the last unit time length τ in the duration of each state. The green, red, and blue shaded parts of Figure 8 show the steady state of unloaded, loaded, and released states.

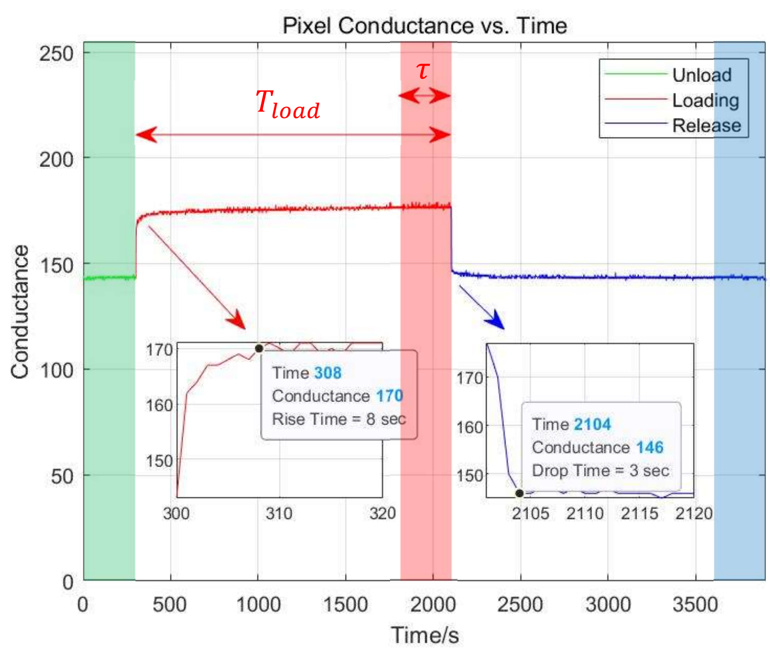

Figure 8. Schematic diagram of the analog reading G curve with time. Shown as a continuous collection of unloaded $T_{unl} = 5$ minutes, then loaded for $T_{load} = 30$ minutes, and then released for $T_{rel} = 30$ minutes. The green, red, and blue curves represent the analog reading G values in the unloaded, loaded, and released states, respectively. The green, red, and blue shaded parts represent the steady state of unloaded, loaded, and released states for a unit time length τ.

Whether the element undergoes plastic deformation before and after loading is also concerned. The difference $diff$ between the unloaded state and the released state is defined as:

$$diff(\%) = \frac{|\overline{G_{unl}} - \overline{G_{rel}}|}{\overline{G_{unl}}} \times 100\% \tag{3.5}$$

We are interested in how long it takes for an element's G to reach an acceptable value. Three quasi-static responses are defined to show the performance of the sensor array analog reading G. Without loss of generality, the acceptable G value is a percentage of the steady-state value, noted by μ. In our experiment, $\mu = 80\%$ (or 90%) is used as the percentage. Rise transient t_r of the element G from the start of loading until it rises to the acceptable G value is defined as:

$$t_r = \underset{i \in T_{load}}{argmin}\ G_{load}(i) \geq \mu_{load}(\overline{G_{load}} - \overline{G_{unl}}) + \overline{G_{unl}} \tag{3.6}$$

Similarly, fall transient t_f of the element analog reading G from the start of release until it falls to the acceptable G value is defined as:

$$t_f = \underset{i \in T_{rel}}{argmin}\ G_{rel}(i) \leq \overline{G_{load}} - \mu_{rel}(\overline{G_{load}} - \overline{G_{rel}}) \tag{3.7}$$

t_r and t_f as the quasi-static response, we are most concerned about are shown in Figure 8. Stability is the relative difference between the G value and the steady-state value is less than a percentage, noted by δ. In our experiment, $\delta = 10\%$ is used as the threshold. Settling transient t_s is defined as the element analog reading G from the start of the state to reach and stabilize at δ of $\overline{G_{load}}$ or $\overline{G_{rel}}$:

$$t_s = \underset{i \in T_{state}}{argmin} \frac{(G_{state}(i) - \overline{G_{state}})}{\overline{G_{state}}} \leq \delta_{state}$$
$$for\ all\ t_s \leq i \leq T_{state} \tag{3.8}$$

To obtain the steady-state element analog reading G in the three states of unloaded, loaded, and released, unit time τ needs to be set. The difference between the mean for 5 minutes and 60 minutes of the unloaded state is less than 0.1%. So $\tau = 5(\text{mins})$ is considered to be an appropriate value, short enough not to waste time and enough to reflect the steady state. The unloaded state only records a unit time length $T_{unl} = \tau = 5(\text{mins})$. Taking into account the situation of long-term use, the loaded and released states collect the total time length is $T_{load} = T_{rel} = 30(\text{mins})$ to observe their changes. In the long-term pressure application, there will always be a period of a slow rise in analog reading G, which is unnecessary for collecting pressure image data sets. Therefore, compared to the released state, set $\mu_{load} = 80\%$ to eliminate the interference of the slow rise of the loaded state. Due to the low resolution of Arduino Nano (8-bit ADC), the analog reading G will oscillate even in steady state. This kind of oscillation is acceptable, and what we care about is whether there is a general tendency for the analog reading G. $\delta_{state} = 10\%$ is set to eliminate the influence of oscillation, and the main measurement is when the general trend of change ends. The settings of these parameters are shown in Table 1.

Table 1. Parameter setting of sensor array performance measurement.

τ (mins)	T_{unl} (mins)	T_{load} (mins)	T_{rel} (mins)	μ_{load}	μ_{rel}	δ_{state}
5	5	30	30	80%	90%	10%

Using the setup shown in Table 1, four pixels of the index (5,1), (10,1), (15,1), and (20,1) were tested under a force of 100 Newtons. 65-minute pixel G change curve is shown in Figure 9, and the performance measurement results shown in Table 2 were obtained.

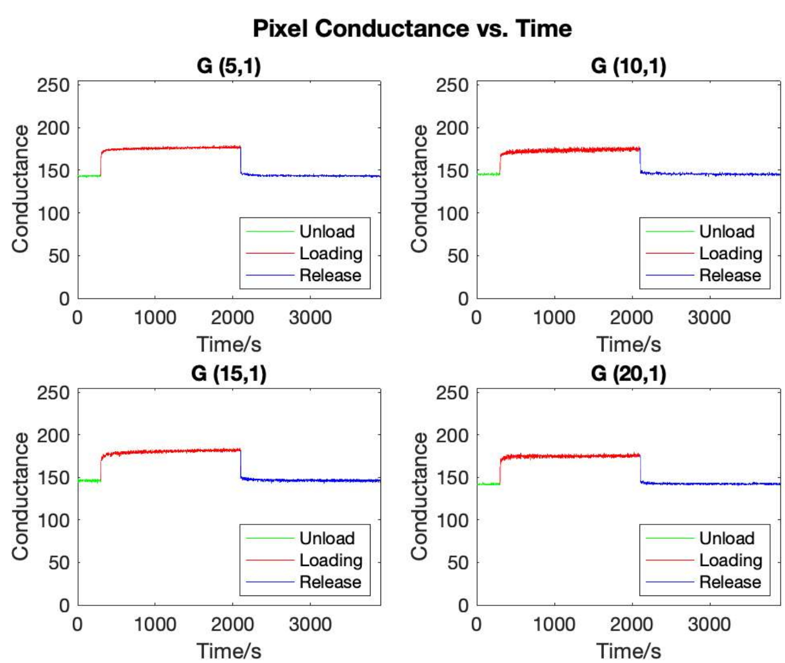

Figure 9. Analog reading G change curve of four pixels in three states. The green, red and blue curves are unloaded, loaded, and released states, respectively.

Table 2. Performance of four pixels analog reading G under unloading, loading, and release states.

	$\boldsymbol{G}(5,1)$	$\boldsymbol{G}(10,1)$	$\boldsymbol{G}(15,1)$	$\boldsymbol{G}(20,1)$
G_{unl}	143.1967	145.1033	146.5367	141.9467
		Loading		
$\overline{G_{load}}$	176.6200	174.5400	181.8167	175.5233
G_{p-load}	179	178	184	179
$t_r(s)$	8	10	13	8
$t_{s-load}(s)$	1285	1789	1105	1773
		Release		
$\overline{G_{rel}}$	143.8339	145.5847	146.7375	142.2259
G_{p-rel}	142	143	143	140
$t_f(s)$	3	2	4	2
$t_{s-rel}(s)$	89	28	96	38
$diff(\%)$	0.44	0.33	0.14	0.20

To ensure the diversification of the data set, a lower sampling rate and appropriate sampling time are essential. The lower sampling rate is set to 1 sample/sec in our experiment. Appropriate sampling rate needs to ensure the number and difference of pressure images in the data set, which can be determined by t_r. Figure 9 and Table 2 show that in the first $t_r = 10$ seconds, the analog reading G quickly rises to an acceptable value. t_{s-load} of each element is greater than 1000 seconds, which proves that the analog reading G rises slowly under long-term pressure, and this rise is small enough to be ignored. In order to avoid repeated pressure images and the element rising to an acceptable value, the collection time is defined as 10 seconds to ensure the diversity and universality of the pressure image data set. Based on these facts, the second experiment setup is proposed as the following.

Experiment Setup 2: Collection Time. *Only the first 10 seconds of pressure images should be continuously recorded.*

In order to ensure that the pressure images are collected with the same initial conditions each time, it is essential to release them after the sensor array is used. The release time is usually specified by t_d and t_{s-rel} in Figure 9 and Table 2, t_f is less than 5 seconds, and t_{s-rel} is less than 100 seconds. In order to reduce unnecessary waste of time, the pressure images are collected for 10 seconds (experiment setup: collection time) and then performed a short release. Such a collection action lasted 30 minutes and then performed a long release. This short release is given by t_d, and the long release is given by t_{s-rel}. We slightly extend both release transient t_d and t_{s-rel} to ensure that each element on the sensor array is released enough. The short release time is defined as 5 seconds, and the long release time is defined as 100 seconds. The difference between unloaded and released is given by $diff$. It can be seen that the difference of each element is less than 1%, which shows the excellent repeatability of the sensor array. So, the third experiment setup is stated below.

Experiment Setup 3: Release Time. *After continuous collection of images each time, 5 seconds are required to release. After 30 minutes of collection, an additional 100 seconds must be released.*

The entire system, including the sensor array and signal processing subsystem, only costs approximately 45 US dollars and demonstrates considerable characteristic parameters, as shown in Table 3.

Table 3. Velostat sensor array characteristic parameters.

Preset Pressure	Resolution	t_r	t_f	t_{s-load}	t_{s-rel}
60 N	1 Pixel/5 mm	$\approx$10 s	$\approx$5 s	$>$ 1000 s	$<$ 100 s

Comprehensive characterization of the Velostat sensor array has been conducted prior to signal processing of the acquired pressure images in the three experiment setups.

CHAPTER FOUR

APPLICATION IMPLEMENTATION AND CLASSIFICATION

4.1 Overview

In this chapter, according to the Velostat sensor array design and fabrication method in Chapter Three, we fabricated three applications to verify the feasibility of the Velostat-based pressure sensing system. In order to effectively identify pressure images, a convolutional neural network ResNet-PI is proposed as an image classification algorithm. Contrast enhancement has been shown to be an effective data preprocessing method in our previous work, which is capable of weighting different pixels.

Based on the proposed design in Chapter Three, we fabricated three applications: an Object Recognition Board, a Smart Cushion, and a Smart Bed Sheet. Data collection was then performed according to the three experiment setups. ResNet-PI is used to train on three datasets respectively and implement different classification tasks. Human-related tasks such as sitting posture recognition and sleeping posture recognition are considered more challenging. The dataset was collected multiple times to obtain a ResNet-PI model with more diversity and temporal universality. Secondary validation is proposed to verify the accuracy of the model in real-time applications.

4.2 Contrast Enhancement

Since the piezoresistive material Velostat can be regarded as resistant in both the unloaded and loaded state, the analog reading G of the sensor array is non-zero even in the unloaded state. Moreover, due to the fabrication differences of the sensor array, electrical noise, and different element positions, the initial analog reading G of each pixel is different. In order to initialize the bias on each pixel and prevent the analog reading G

from becoming negative, the analog reading G of each pixel has been continuously collected for a period of time in advance to calculate the mean and standard deviation. Each pixel's original analog reading G subtracts the mean to initialize the bias and then adds four standard deviations to prevent it from becoming negative.

$$\boldsymbol{G}'(i) = \boldsymbol{G}(i) - \boldsymbol{Mean} + 4\boldsymbol{Std} \tag{4.1}$$

where $\boldsymbol{G}(i)$ is the original analog reading G matrix of the sensor array at the i-th moment. $\boldsymbol{G}'(i)$ is the initial analog reading G matrix after the bias is eliminated at the i-th moment. $\boldsymbol{Mean}$ and $\boldsymbol{Std}$ are respectively the mean and standard deviation of the analog reading G matrix collected for a period of time (1 hour) in advance. In order to apply contrast enhancement to pressure images, we first need to initialize the pixel analog reading G. Only nine pixels of analog reading G are shown here for discussion. Table 4 shows the detailed information of these 9 pixels analog reading G.

Although the low variance and standard deviation (less than 1) show that the sensor array is very stable in the unloaded state, due to sensor fabrication and electrical noise, each pixel analog reading G mean on the sensor array is unevenly distributed in the interval 136 to 149. This uneven distribution and high bias will affect the sensitivity and recognition accuracy of the pressure image. Equation (4.1) is used here to subtract bias and initialize the sensor array.

After obtaining the initialized analog reading G matrix through (4.1), the next step is to enhance the contrast between the signal and noise in the pressure image. We assume that the output span of pixel analog reading G is divided into a low output span and a high output span.

Table 4. Average, variance and standard deviation of nine pixels analog reading G.

Pixel Coordinates	Mean	Variance	Standard Deviation
G (1,1)	143.1069	0.5979	0.7732
G (1,10)	141.9957	0.4233	0.6506
G (1,20)	146.1117	0.3794	0.6160
G (10,1)	145.7284	0.4498	0.6707
G (10,10)	142.1016	0.1207	0.3475
G (10,20)	143.9753	0.2105	0.4588
G (20,1)	146.7424	0.4633	0.6806
G (20,10)	142.7388	0.3435	0.5861
G (20,20)	145.2029	0.4600	0.6782

As the pressure increases, the pixel analog reading G increases and moves from the low output span to the high output span. At the same time, the distribution of electrical noise remains unchanged. What we can expect is that there is a high amount of electrical noise and a low amount of signal in the low output span. Conversely, there are a high amount signals and a low amount of noise in the high output span. The essence of the designed contrast enhancement is to increase the high output span while maintaining or weakening the low output span.

We have selected three candidate functions. One Boolean function is the thresholding, and two nonlinear scaling functions are power and exponential.

Thresholding is our priority as the simplest way to increase the contrast. The formula for thresholding can be expressed as:

$$\boldsymbol{G}''_{\mathrm{thld}}(i) = \begin{cases} 255 & , \boldsymbol{G}'(i) \geq \gamma \\ 0 & , \boldsymbol{G}'(i) < \gamma \end{cases} \tag{4.2}$$

where $\boldsymbol{G}''_{\mathrm{thld}}(i)$ is the threshold contrast enhanced analog reading G matrix of the sensor array at the i-th moment. γ is a custom threshold coefficient to be tested for the best result. Thresholding needs to traverse each pixel in $\boldsymbol{G}'$, if the pixel value is greater than γ, it is signal, and if it is less than γ, it is noise. Power and exponential are used as common nonlinear scaling functions, and they directly calculate $\boldsymbol{G}'$. The formula of power can be expressed as:

$$\boldsymbol{G}''_{\mathrm{power}}(i) = \boldsymbol{G}'^{\alpha}(i) \tag{4.3}$$

where α is a custom power coefficient to be tested for the best result. The formula of exponential can be expressed as:

$$\boldsymbol{G}''_{\exp}(i) = e^{\beta \boldsymbol{G}'(i)} \tag{4.4}$$

where β is a custom exponential coefficient to be tested for the best result. After getting the initialized pressure image, Equation (4.2), (4.3), and (4.4) is used to enhance the contrast of the pressure image. According to the original pressure image data set, the initialized pressure image analog reading G changes from 0-5 (low output span) when unloaded and changes from 5-15 (high output span) when loaded.

Although contrast enhancement can effectively attach different weights to the low output span and high output span, the classification accuracy is high enough without contrast enhancement due to the convolutional neural network's powerful automatic feature extraction capability. There are some difficulties in using contrast enhancement to improve the classification accuracy, such as choosing the appropriate coefficient. In previous work, we used an exhaustive method to find the most suitable coefficients. However, the coefficients found by this method are limited, and they can only be used in specific data sets. So, in this thesis, contrast enhancement is not used as data preprocessing. It is only used in visualization applications.

4.3 Convolutional Neural Network

CNN has been widely used in computer vision for an object, sitting posture, and sleeping posture recognition. In our experiment, we also apply CNN to pressure images for the CNN can extract feature vectors in the pressure image to calculate the probability of an image's category for matching. Since the size and resolution of the pressure images generated by the three applications are the same, the same CNN architecture is used to train and identify different pressure image datasets, respectively.

To use CNN to classify these objects, a residual neural network based on ResNet18 [74] was developed. Figure 8 shows the block diagram of the modified version of ResNet for Pressure Image (ResNet-PI) in this work. To make the neural network more suitable to the collected pressure images (with a low resolution of 27×27×1) in this work, a simplified ResNet-PI scheme modified from ResNet-18 is adopted to reduce the number of convolutional layers and CNN parameters for a more lightweight CNN architecture. In particular, the Dropout layer was added to ResNet-18, as shown in the purple block in Figure 10. The dropout layer can prevent the model from overfitting and make the model more generalizable. In ResNet-PI model, the Dropout rate is set to 0.2.

ResNet-PI is implemented in TensorFlow. To detail the configuration, the size of the initial convolutional layer is set as 3×3, the stride as 1, the number of initial filters as

16, and the total number of layers as 14. With such a lightweight CNN and low-resolution image data set framework, this configuration not only guarantees overall performance sufficient to our requirements but also provides a potential real-time solution for other human-related applications. The initial learning rate is 10^{-3}, learning rate becomes 0.1 times the initial learning rate after every 100 epochs of training. A total of 200 epochs are trained. The batch size is 32, and the selected loss function is classification cross-entropy.

ResNet-PI has 3 ResNet layers, and each ResNet layer has two basic blocks (dashed blocks). The ResNet layer is distinguished by different fill colors (blue, red, yellow), and down-sampling (dashed line) is required between the two ResNet layers. In order to save space, only the first basic block is drawn completely. Each basic block is composed of 2D Convolution Filter (Conv), Rectified Linear Unit (ReLU), Batch Normalization (BaN), and Dropout. The two layers are connected by the skip layer. Finally, the output of the ResNet layer performs the Average Pooling (Avg Pool) operation and uses Dense to output the label of the object.

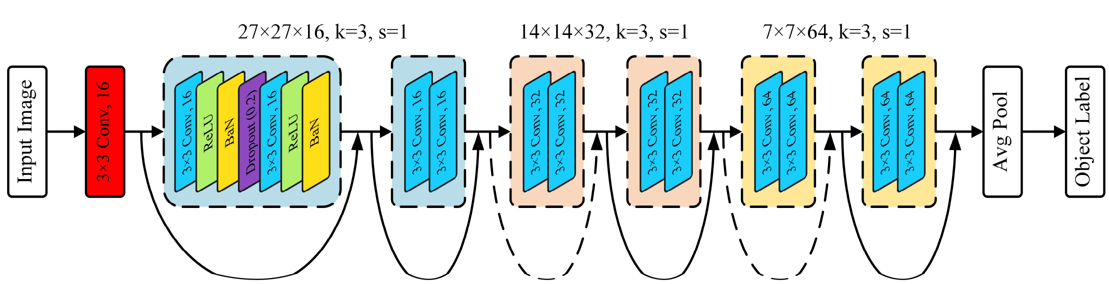

Figure 10. ResNet-PI architecture block diagram.

4.4 Object Recognition Board

According to the structural design of the general Velostat sensor array in Chapter Three, the protective layers of the Object Recognition Board are covered with a 0.0127 mm polyvinyl chloride (PVC) protective film. This protective film is transparent, soft, thin, and cheap. It not only maintains the robustness of the sensor array but also does not weaken the pressure signal of the object. Figure 11 annotates the size and resolution of the Object Recognition Board.

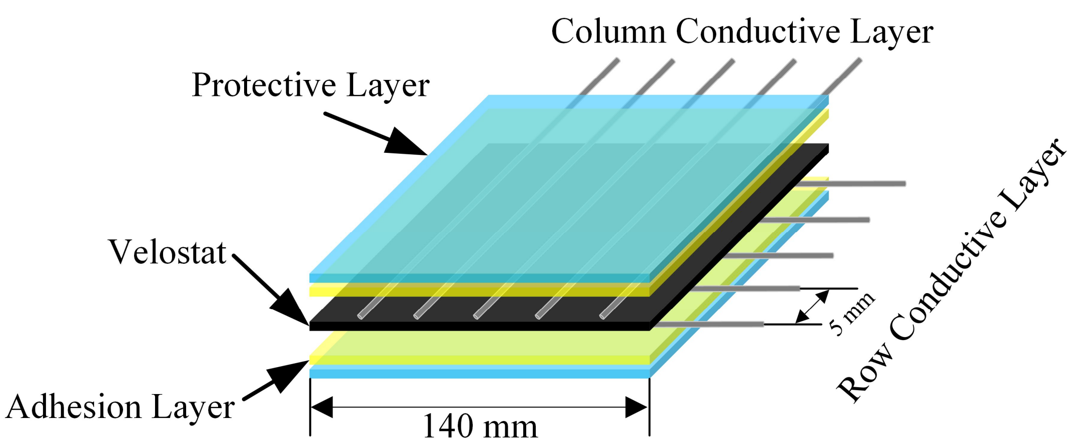

Figure 11. Schematic diagram of the Object Recognition Board.

For easy movement, better performance, and robustness, the Object Recognition Board is placed on a hard wooden board. Figure 12 shows the overall Object Recognition Board, including the PCB and sensor array, used to collect object pressure information.

We have selected ten objects for data collection, with seven objects that are distinguishable shape numbers made by LEGOs, and three objects from daily life, including an iron block, a Pepsi can, and a Perrier bottle, as shown in Figure 13. These objects were chosen because of their rigidity, distinguishable contours, and low surface area characteristics. Combining three experimental setups, the pressure image data set was collected by placing these objects at different positions in the Velostat sensor array at different rotation angles.

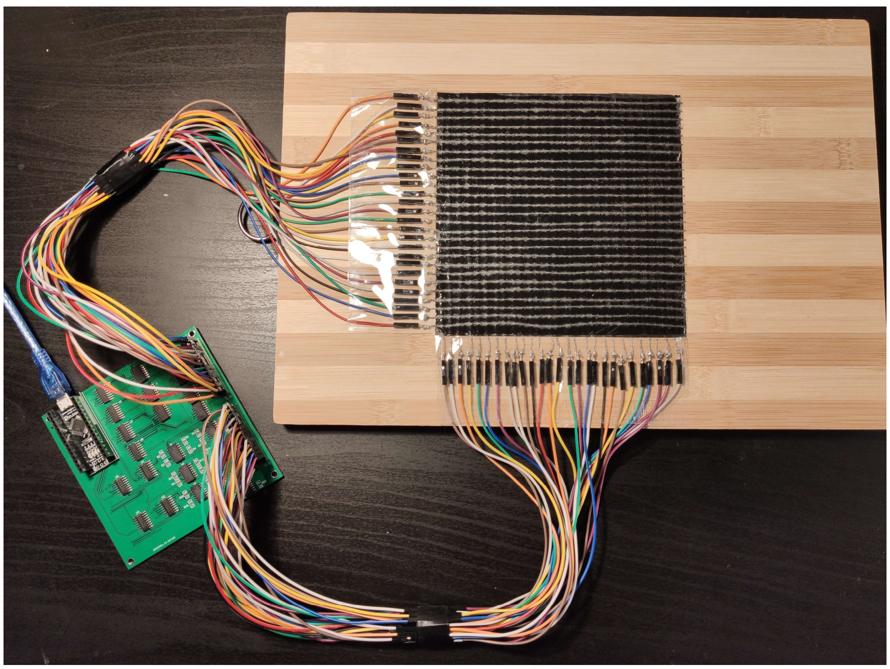

Figure 12. Object Recognition Board.

We collected 8066 original pressure images of 10 objects. Following experiment setup: object weight, these ten objects have been added with additional pressure to reach 60 Newtons. When collecting pressure images, follow the collection time in experiment setup: collection time and the release time in experiment setup: release time. Besides, the original data set was expanded four times by rotation and translation.

The whole data set has 32264 pressure images, which is divided into the training data set (22584 images) and test data set (9680 images) at a ratio of 7:3. Figure 14 shows the pressure image of ten objects after contrast enhancement. These images are only to provide visual application prospects and will not be used for the training of ResNet-PI. It can be seen that the objects pressure characteristics are clearly visible even in the case of low resolution and noise.

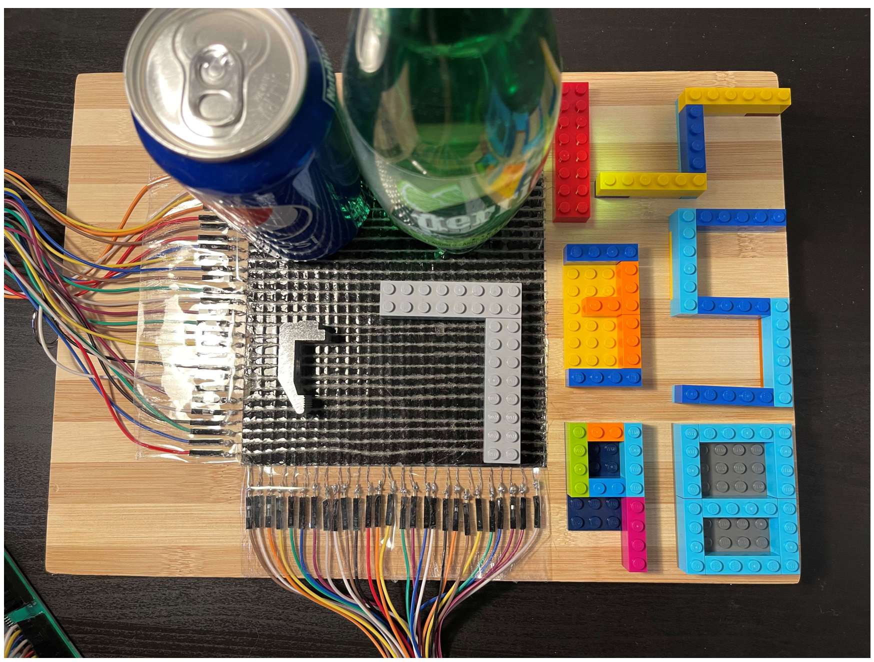

Figure 13. Ten objects were used to collect object pressure information. The order from left to right and top to bottom is Pepsi, Perrier, one, two, iron block, seven, three, five, nine, eight. Since four, six, and nine are easily confused, only one of them is selected. Pepsi, Perrier, and iron block collect the bottom pressure image in the direction shown in the figure. Seven LEGO numbers are flipped to collect pressure images of the numbers side.

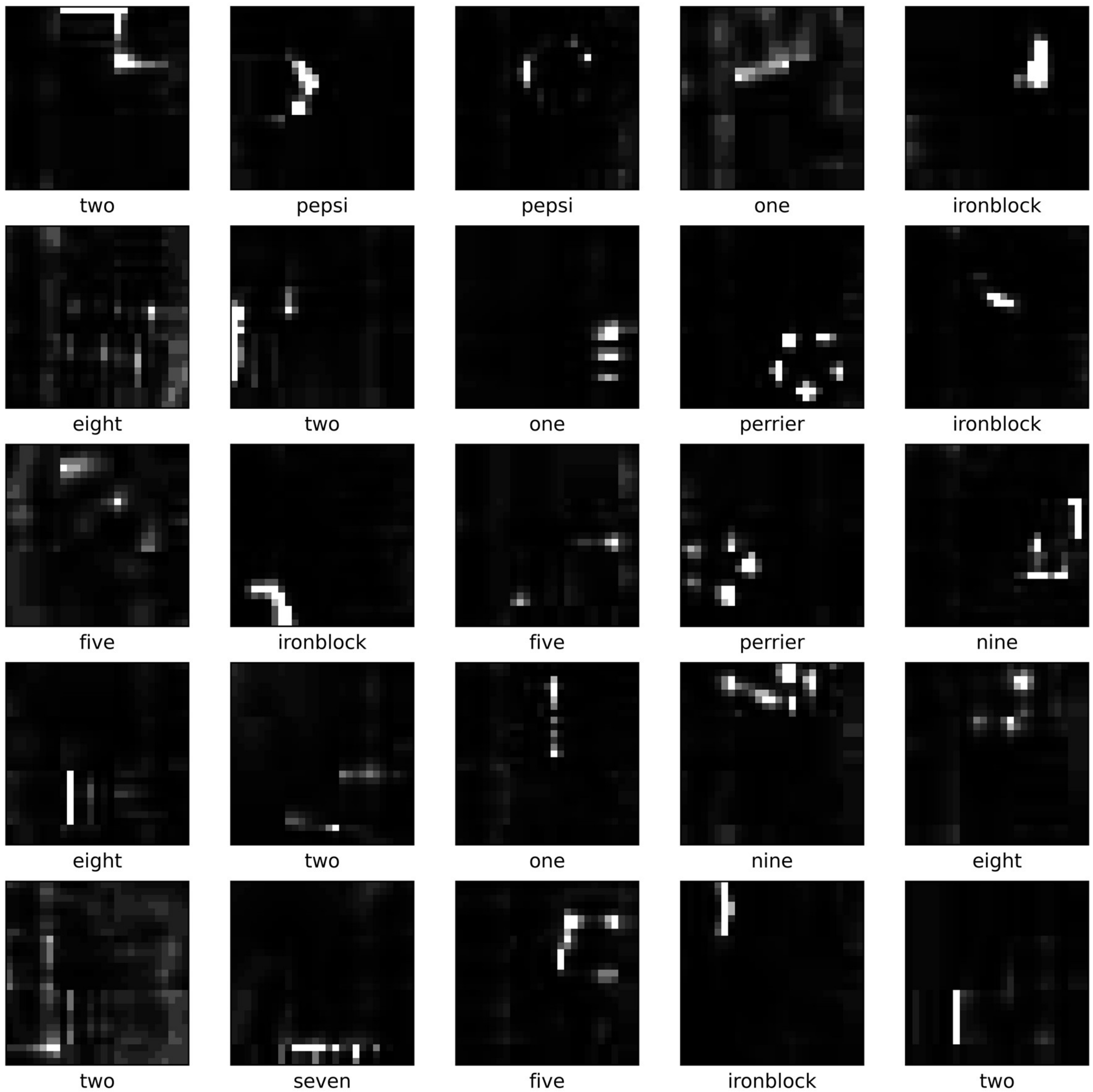

Figure 14. Pressure images of ten objects after contrast enhancement.

The confusion matrix is shown in Figure 15, which can be seen that most of the errors come from similar object pressure images, such as "three" with "eight" and "five" with "eight" have been confused. The main reason may be that the resolution of the fabricated sensor array is not high (the distance between the two pixels is approximately 5 mm), and the edge features of objects may be in the blank area between two elements. Figure 16 (a) and Figure 16 (b) show the accuracy curve and loss curve of the model, respectively. The obvious convergence and close match of the processed data to the training model validate that our model parameter settings are appropriate for such an application.

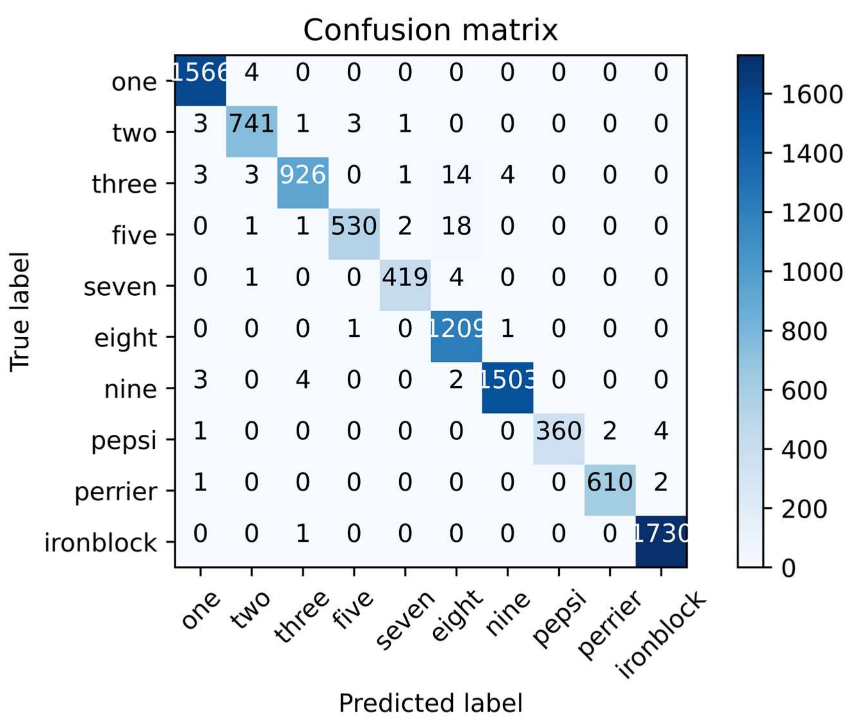

Figure 15. Confusion matrix for ResNet-PI recognizing ten objects.

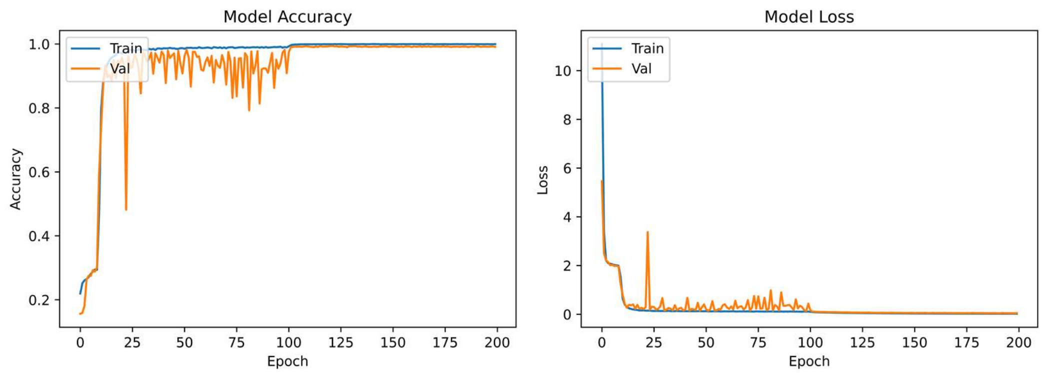

(a) (b)

Figure 16. ResNet-PI training model for 10 objects, (a) model accuracy curve, (b) model loss curve.

To highlight the advantages of the ResNet-PI we designed, Table 5 compares several common image classification algorithms. It can be seen that the pressure image data set generated by our Velostat sensor array has distinguishability, which can work on multiple popular CNNs and achieve valuable accuracy. Also, it can be observed that with a much simplified and light weighted scheme configured to our Velostat sensor array, ResNet-PI demonstrates a remarkable accuracy that's comparable to some other popular CNNs. The performance suggests its great potential in many other human-related applications where real-time classifications are highly desired.

Table 5. Comparison of accuracy between ResNet-PI and four other classification algorithms.

ResNet-PI	AlexNet [49]	VGG19 [50]	ResNet-50 [51]
0.9914	0.9923	0.9659	0.9912

4.5 Smart Cushion

Smart Cushion has the same structure as the Object Recognition Board, but 100% cotton cloth is chosen as the protective layer material because of its firmness, comfort, and low price. Compared with PVC protective film, cotton cloth is sturdier and more suitable for human sitting activities. Figure 17 (a) shows the designed human sitting posture collection system. When the human body sits on the Smart Cushion, Velostat receives different human body pressure distributions and produces different resistance distributions. In order to ensure that the initial conditions of the experiment remain unchanged, when each sitting posture of the subject is collected, the relative position of the laboratory seat and the Smart Cushion should be kept unchanged. For this reason, we use tape to fix the Smart Cushion and the PCB on the laboratory chair seat and backrest, as shown in Figure 17 (b) and Figure 17 (c), respectively. The pressure sensor array made by Velostat is made in the middle of the Smart Cushion, leaving room around for conductive threads. According to experience and previous literature, the Smart Cushion is placed in the area where the human body contacts the laboratory chair seat and generates the most significant pressure, as shown in Figure 17 (d).

Based on daily life experience and previous literature, we set up five sitting postures: (a) normal, (b) forward, (c) backward, (d) left & right, (e) upright, as shown in Figure 18. These five sitting postures all change from the "normal" sitting posture, and "forward" represents thinking in daily activities, and the body's center of gravity moves forward. "Backward" stands for rest and the center of gravity of subject moves backward. "Left & right" represents a relaxed and lively left and right cross-legged posture, and people usually appear in this sitting posture when watching TV and movie.

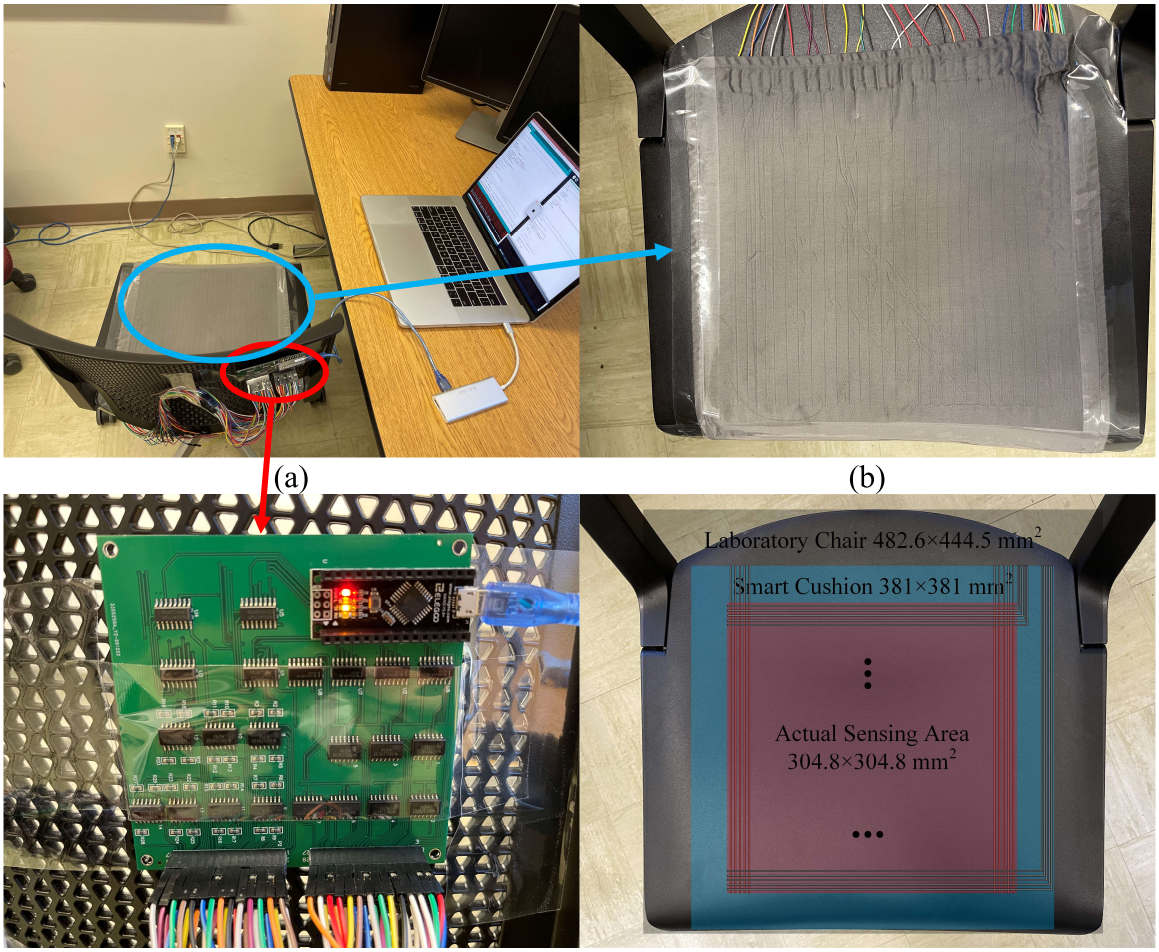

(a) (b) (c) (d)
Figure 17. Human sitting posture collection system. (a) Overall sitting posture collection system includes the Smart Cushion, signal processing subsystem PCB and a host computer, (b) the Smart Cushion fixed on the laboratory chair seat, (c) the signal processing subsystem PCB fixed behind the laboratory chair backrest, (d) schematic diagram of the Smart Cushion structure.

"Upright" represents a sitting posture that is usually tense and attentive when listening to a lecture. At this time, only half of the buttocks are on the chair, and the position of the caudal vertebra will move forward. The "upright" sitting posture deliberately changes the position of the caudal vertebrae to meet the requirements of various sitting posture recognition tasks.

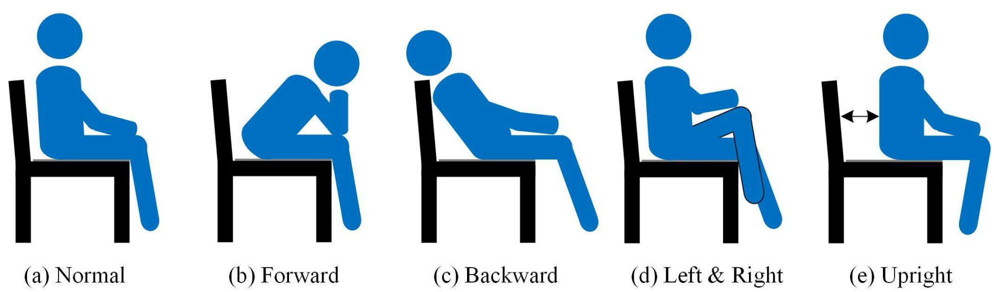

Figure 18. Schematic diagram of 5 sitting postures in human daily activities, (a) normal, (b) forward, (c) backward, (d) left & right, (e) upright.

In our experiment, human sitting posture data collection followed the experimental setup in the previous study. When the subjects sat down and adjusted their posture, they began to collect 10 seconds of data continuously, and the sampling frequency was 2 samples/sec. After every 10 seconds of continuous data collection, the subject needs to stand for at least 5 seconds, and release at least 100 seconds in the middle of each posture to make the Smart Cushion release to its initial state. Figure 19 shows the pressure image of the subject's "normal" sitting posture, and the contours of the thighs and the areas of different pressure distribution can be clearly seen, which shows the prospect of the Smart Cushion in visualization applications. Again, Figure 19 is just for visualization purposes, and only raw pressure images are used for ResNet-PI training.

In general, a trained CNN model usually performs better on a dataset that is not sufficiently diverse, and the CNN model will overfit in this case. Such a CNN can only fit the data well on the training data. Although it is evident that our pressure images have huge noise and ResNet-PI also uses Dropout layers to avoid overfitting, we noticed that the trained ResNet-PI does not perform well in developing real-time applications.

Figure 19. The pressure image of the subject's "normal" sitting posture after contrast enhancement, filtering, and resizing.

Unlike the Object Recognition Board, the pressure images generated by the Smart Cushion cannot be rotated and flipped to expand the number of pressure images for a more diverse dataset. The pressure distribution generated by the human sitting posture always has the same orientation (people do not sit facing the backrest). We believe that the main reason for low diversity is that the subject’s muscle memory when the sitting posture is collected leads to the singularity of the sitting posture in the data set, and the sitting posture when the real-time application is developed a few days later is quite different from the original data set. The secondary reasons include changes in the subject's weight, laboratory temperature, the initial state of the Smart Cushion, and the electrical resistance of the Smart Cushion after long hours of work.

To obtain a time-universal ResNet-PI model suitable for real-time applications, we collected sitting postures at different times to generate the dataset. We collected four datasets at different times in two days, with an interval of six hours between each data set to obtain diverse pressure images. These four datasets are all collected with 500 (samples/dataset/posture), a total of 10,000 sitting posture images dataset for ResNet-PI training. Then on the third day, 100 (samples/posture) were collected, a total of 500 sitting posture images secondary validation dataset was used to test the temporal universality of the Smart Cushion.

Figure 20 (a) shows that the sitting posture test dataset collected multiple times has a confusion matrix with an accuracy of 1.0. Figure 20 (b) shows that the secondary validation dataset has a confusion matrix with an accuracy of 0.9660. It can be seen that the trained ResNet-PI model possesses high accuracy even for the data collected on the third day, which demonstrates the temporal universality and diversity of the model.

4.6 Smart Bed Sheet

Compared with the Object Recognition Board and the Smart Cushion, the Smart Bed Sheet is changed on the basis of the Smart Cushion in order to meet the large area requirement of human sleeping posture and the low fabrication price. According to the previous discussion of the Velostat sensor array, the pressure distribution represented by the pressure image is only related to the resistance of the Velostat at the intersections of the row and column conductive threads (pressure sensor elements) and the pressure distribution between the elements is not valid.

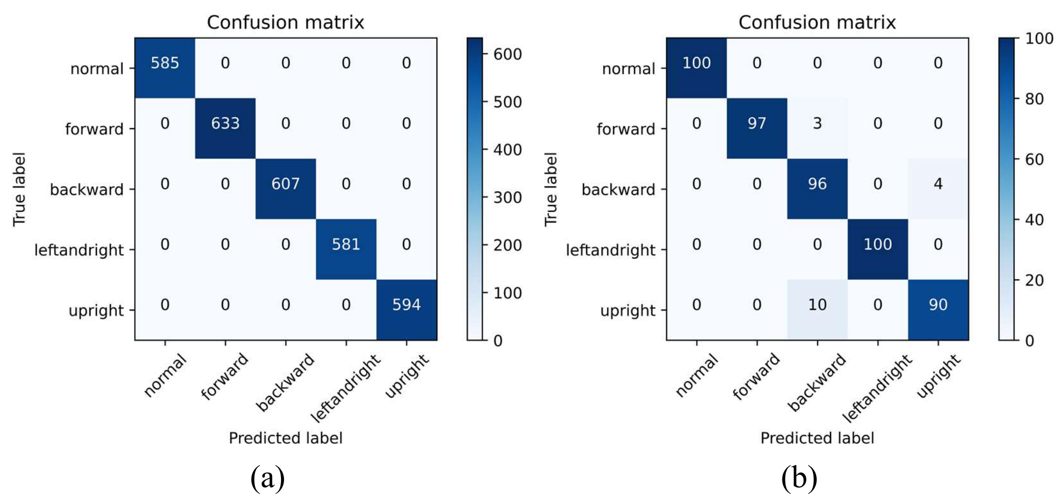

Figure 20. Confusion matrix of sitting posture recognition, (a) test dataset, (b) second validation dataset.

Therefore, we use separated Velostat sensor elements as shown in Figure 21, which has three advantages: saving material, avoiding stray current flowing through the Velostat resistance material to adjacent elements, and avoiding the deformation caused by human body pressure to affect adjacent elements through the material. The design approach of separated Velostat sensor elements can reduce the use of Velostat material by 64%.

Figure 21 (a) shows the structure, size, and actual sensing area of the Smart Bed Sheet. Unlike the Object Recognition Board and the Smart Cushion, the distance between sensor elements in the vertical and horizontal directions of the Smart Bed Sheet is not equidistant, as shown in Figure 21 (b). In order to conform to the length and width of the human body when lying on the bed, the size of the Smart Bed Sheet is set to be equal to the Queen size, and the actual sensing area will be slightly smaller than the bed sheet.

Figure 22 (a) shows the Smart Bed Sheet placed on a Queen size mattress for collecting subject sleeping posture data. The fabricated Smart Bed Sheet is flexible, soft, and portable, and Figure 22 (b) shows its foldability and low weight.

Referring to daily life experience and previous literature, we set up four sleeping postures: (a) supine, (b) prone, (c) left lateral, (d) right lateral, as shown in Figure 23. These four sleeping postures are mainly defined by the chest orientation, which is up, down, left, and right, respectively. To ensure the diversity of the pressure image dataset, subjects were asked to perform data collection on the Smart Bed Sheet as in daily sleep, which included acceptable translation and rotation of the subject's body relative to the Smart Bed Sheet. In addition to the position of the subject's body on the Smart Bed Sheet, the rotation and bending of the subject's limbs relative to the body were also acceptable, as shown in Figure 23.

On the basis of following three experimental setups, the sampling period was set to 5 seconds, and the sampling frequency was set to 2 samples/sec. Between each sampling period, subjects were asked to leave the Smart Bed Sheet for at least 5 seconds and then lie down in a different relative position and rotation. One thousand periods were collected for each sleeping postures, so a total of 40,000 sleeping posture pressure images dataset were collected.

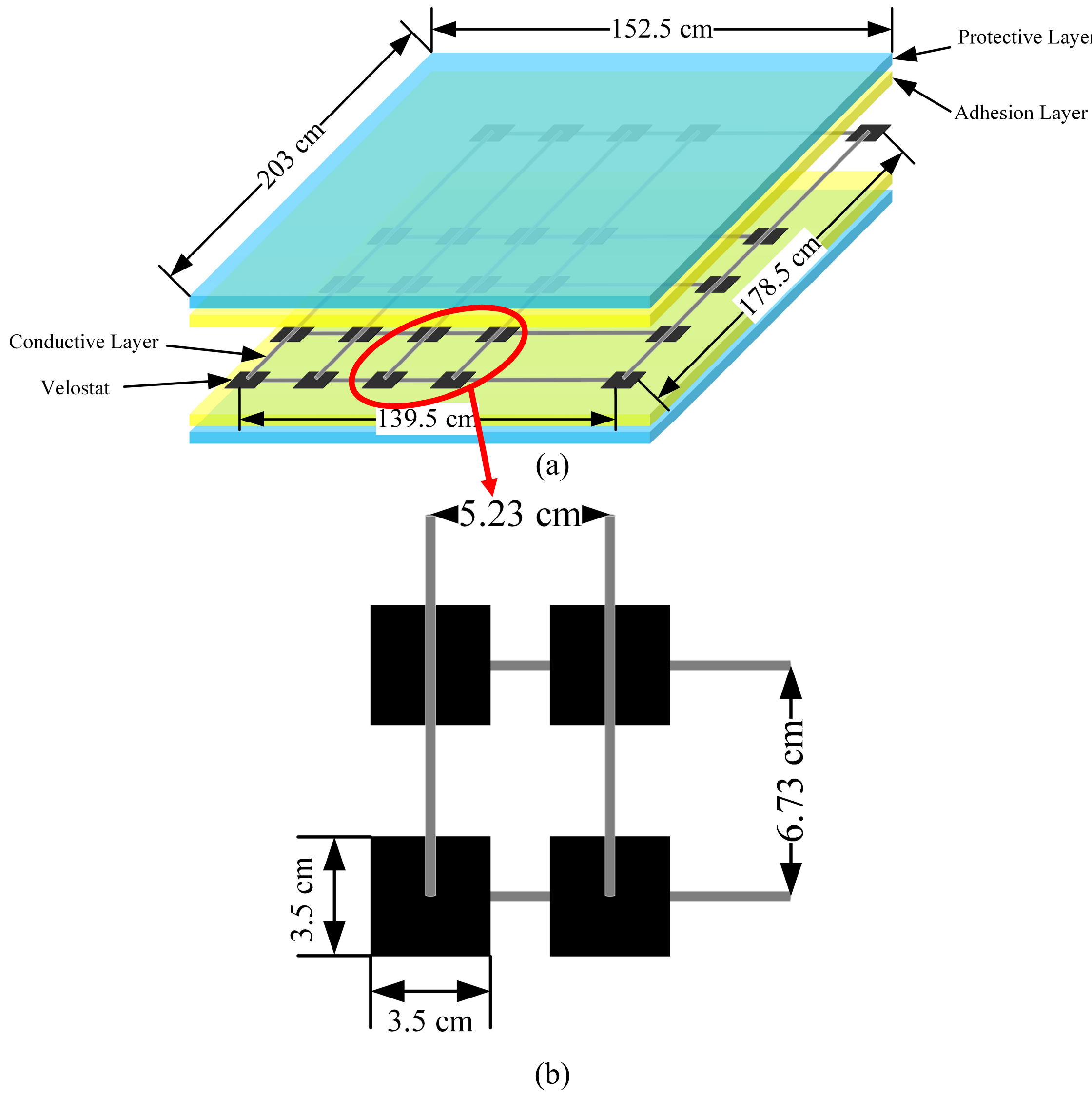

Figure 21. Schematic diagram of the Smart Bed Sheet, (a) structure, size, and actual sensing area, (b) separated sensor elements size and spacing.

(a) (b)

Figure 22. Actual image of the Smart Bed Sheet. (a) Smart Bed Sheet is placed on a Queen size mattress, (b) The Smart Bed Sheet is folded and the total weight is 2749 grams.

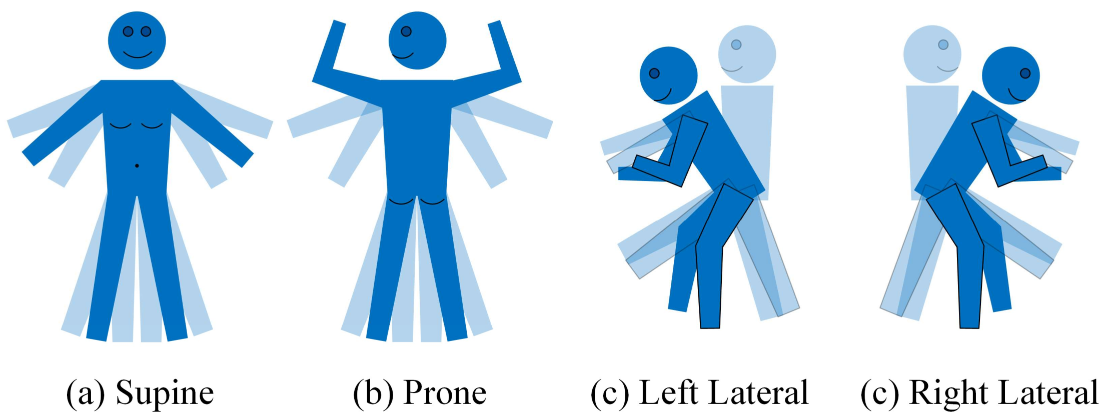

Figure 23. Schematic diagram of four sleeping postures, (a) supine, (b) prone, (c) left lateral, (d) right lateral. The subjects' diverse sleeping postures are indicated by the shaded bodies.

Figure 24 shows the pressure image of the subject's "supine" sleeping posture, and the human body pressure distribution can be clearly seen, which shows the prospect of the Smart Bed Sheet in visualization applications. Again, Figure 24 is just for visualization purposes, and only raw pressure images are used for ResNet-PI training.

Using a similar strategy as for sitting posture recognition, data collection for sleeping posture also follows the diversity and temporal universality approach. The dataset used for training was collected at different times over multiple days, a total of 10,000 sleeping posture images dataset for ResNet-PI training. In addition to this training dataset, a secondary validation dataset was collected the following day to verify the temporal universality of the Smart Bed Sheet.

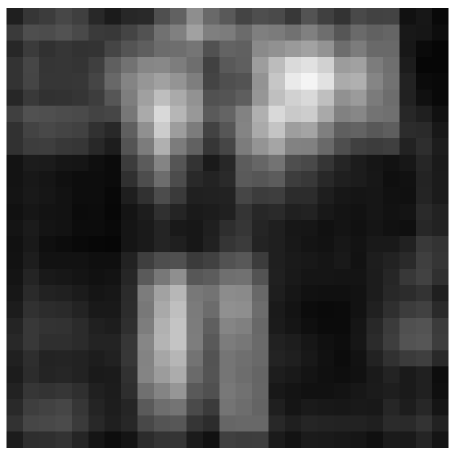

Figure 24. The pressure image of the subject's "supine" sleeping posture after contrast enhancement, filtering, and resizing.

Figure 25 (a) shows that the sleeping posture test dataset collected multiple times has a confusion matrix with an accuracy of 1.0. Figure 25 (b) shows that the secondary validation dataset has a confusion matrix with an accuracy of 0.9990. It can be seen that the trained ResNet-PI performs well on both the test dataset and the secondary validation dataset, which shows the ability of the model to handle datasets of different times and the prospect of developing real-time applications.

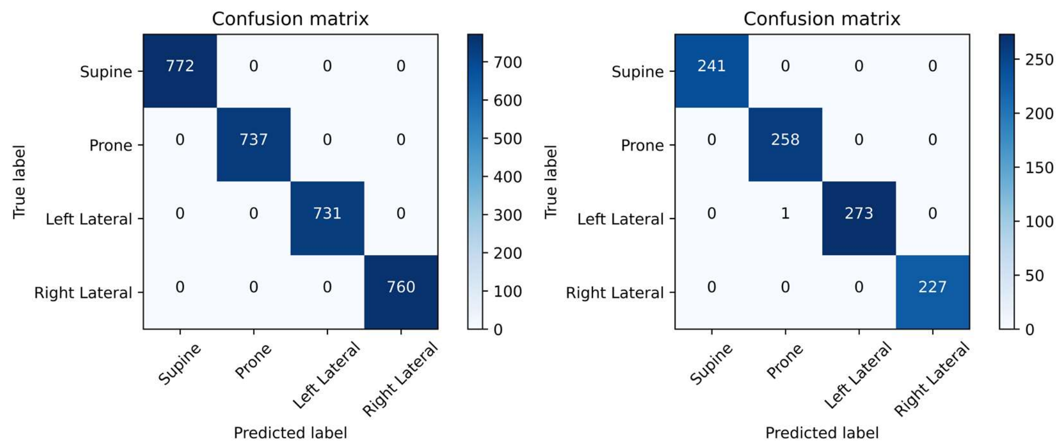

(a) (b)

Figure 25. Confusion matrix of sleeping posture recognition, (a) test dataset, (b) second validation dataset.

According to the high classification accuracy of the three applications, we verified that the generality of the proposed Velostat-based pressure sensing system. The Object Recognition Board, Smart Cushion, and Smart Bed sheet were fabricated to achieve different recognition and classification tasks. Although they have similar structures and materials, they have different sizes and resolutions. Especially the pressure-sensing system also receives different pressure distributions according to different recognition tasks.

The specific characteristics of the proposed Object Recognition Board, Smart Cushion, and Smart Bed Sheet are shown in Table 6. This table shows that our pressure sensing system can develop effective applications at different sizes and resolutions, demonstrating its generality and utility.

Table 6. The specific characteristics of the proposed Object Recognition Board, Smart Cushion, and Smart Bed Sheet.

	Model Size $(mm \times mm)$	Sensing Size $(mm \times mm)$	Resolution $({mm \times mm}/_{Pixel})$	Price (USD)
Object Recognition Board	140×140	140×140	5×5	25
Smart Cushion	381×381	304.8×304.8	11.3×11.3	45
Smart Bed Sheet	2030×1525	1785×1395	67.3×52.3	220

CHAPTER FIVE

CONCLUSION

5.1 Overview of Thesis

In this thesis, a pressure sensing system based on a Velostat sensor array is presented for acquiring and processing pressure image datasets. The system includes a Velostat piezoresistive sensor array, a signal processing subsystem, and a convolutional neural network ResNet-PI for recognizing pressure images. The parameters, such as pressure σ and applied time t that affect the Velostat material and sensor array output are discussed. According to the resistance sensitivity and quasi-static response, three experiment setups are developed, including object weight, collection time, and release time, which can increase the universality, repeatability, and reliability. ResNet-PI was developed to recognize and classify pressure images from three applications: Object Recognition Board, Smart Cushion, and Smart Bed Sheet. In particular, data collection is performed multiple times in human-related applications to increase the diversity and temporal universality of the dataset. ResNet-PI recognized ten objects, five sitting postures, and four sitting postures and achieved the best recognition accuracy of 0.9914, 0.9660, and 0.9990, respectively. In summary, through thorough characterization of Velostat material and sensor array, we have demonstrated that such sensor array can be used for the generation of reliable pressure images. The lightweight ResNet-PI also provides a high-performance, considerable accuracy, and feasible recognition and classification solution for this system.

5.2 Future Directions

What we have demonstrated is that our current framework is a viable solution to the still image recognition task. However, in the real world, most pressure recognition tasks are dynamic tasks, as we discuss in Chapter 1.4. It can be anticipated that with added a special neural network layer for time correlation processing, the system presented in this paper can be readily extended to more human-related applications where real-time pattern recognitions are vital. Generally speaking, this special neural network layer can be Long short-term memory (LSTM), 1D CNN, and fully connected (Dense) layer, etc., which correspond to different processing methods for features. In this dynamic image recognition neural network, ResNet-PIs corresponding to the number of input images first extracts the features of the pressure images, and then a special neural network layer processes the relationship between this series of images. Take LSTM as an example, one of the most popular neural network layers for processing time, it can be used to process a series of outputs of ResNet-PI. In addition to dynamic classification applications, considering the time-varying characteristics of Velostat resistance, noise, subject habits, etc., such a CRNN is a necessary neural network for future real-world applications.

Another future direction is to have more clearly visible, higher contrast, and high-resolution visualization applications. The fabrication of pressure sensor array hardware and related applications presents difficulties, especially in large size and high-resolution applications. However, the increase in size and resolution is limited for recognition accuracy gains due to marginal effects. Current sensor arrays generate pressure images with a resolution of 27×27, which is far from adequate for visualization applications in human activity monitoring. In addition to filtering and contrast enhancement, super-resolution of current pressure images is also a necessary research scheme. Traditional super-resolution methods include bicubic interpolation, deep neural network and, generative adversarial network [82]. Our future direction is to develop a super-resolution generative adversarial network applied to pressure images. This SRGAN-PI achieves super-resolution by learning from our pressure image dataset as well as publicly available high-resolution human lying pose dataset [83]. This high-resolution dataset makes it possible for our system backend to output high-quality monitoring.

REFERENCES

[1] L. Yuan, H. Qu and J. Li, "Velostat Sensor Array for Object Recognition," *IEEE Sens. J.*, vol. 22, no. 2, pp. 1692-1704, Jan. 2022.

[2] L. Yuan, J. Li, "Smart Cushion Based on Pressure Sensor Array for Human Sitting Posture Recognition," *Proc. 2021 IEEE Sens. Conf.*, pp.1-4, 2021.

[3] C. Huang, Q. Wang, M. Zhao, C. Chen, S. Pan, and M. Yuan, "Tactile Perception Technologies and Their Applications in Minimally Invasive Surgery: A Review," *Front. Physiol,* vol. 11, p. 1601, Dec. 2020.

[4] X. Pu, S. An, Q. Tang, H. Guo, and C. Hu, "Wearable triboelectric sensors for biomedical monitoring and human-machine interface," *Iscience,* p. 102027, Jan. 2021.

[5] X. Chen, Y. Mao, X. Ma, and L. Qi, "A Tactile Method for Rice Plant Recognition Based on Machine Learning," *Sensors,* vol. 20, no. 18, p. 5135, Jan. 2020.

[6] A. Dos Santos, E. Fortunato, R. Martins, H. Águas, and R. Igreja, "Transduction Mechanisms, Micro-Structuring Techniques, and Applications of Electronic Skin Pressure Sensors: A Review of Recent Advances," *Sensors,* vol. 20, no. 16, p. 4407, Jan. 2020.

[7] Y. Wang, Y. Lu, D. Mei, and L. Zhu, "Liquid Metal-Based Wearable Tactile Sensor for Both Temperature and Contact Force Sensing," *IEEE Sens. J.,* vol. 21, no. 2, pp. 1694-1703, Aug. 2020.

[8] W. Luo, V. Sharma, and D. J. Young, "A Paper-Based Flexible Tactile Sensor Array for Low-Cost Wearable Human Health Monitoring," *J. Microelectromech. Syst.,* vol. 29, no. 5, pp. 825-831, Aug. 2020.

[9] J. Liang, J. Wu, H. Huang, W. Xu, B. Li, and F. Xi, "Soft sensitive skin for safety control of a nursing robot using proximity and tactile sensors," *IEEE Sens. J.,* vol. 20, no. 7, pp. 3822-3830, Dec. 2019.

[10] L. Zhu, Y. Wang, D. Mei, and C. Jiang, "Development of Fully Flexible Tactile Pressure Sensor with Bilayer Interlaced Bumps for Robotic Grasping Applications," *Micromachines,* vol. 11, no. 8, p. 770, Aug. 2020.

[11] M. I. Tiwana, S. J. Redmond, and N. H. Lovell, "A review of tactile sensing technologies with applications in biomedical engineering," *Sens. Actuators A: Phys.,* vol. 179, pp. 17-31, June 2012.

[12] F. Wen *et al.*, "Machine learning glove using self-powered conductive superhydrophobic triboelectric textile for gesture recognition in VR/AR applications," *Adv. Sci.,* vol. 7, no. 14, p. 2000261, July 2020.

[13] J. Jang, Y. S. Jun, H. Seo, M. Kim, and J.-U. Park, "Motion detection using tactile sensors based on pressure-sensitive transistor arrays," *Sensors,* vol. 20, no. 13, p. 3624, Jan. 2020.

[14] C. Chi, X. Sun, N. Xue, T. Li, and C. Liu, "Recent progress in technologies for tactile sensors," *Sensors,* vol. 18, no. 4, p. 948, Apr. 2018.

[15] X. Luo and Y. B. Gianchandani, "A 100 μm diameter capacitive pressure sensor with 50 MPa dynamic range," *J. Micromech. Microeng.,* vol. 26, no. 4, p. 045009, Mar. 2016.

[16] Q. Tan *et al.*, "A high temperature capacitive pressure sensor based on alumina ceramic for in situ measurement at 600 C," *Sensors,* vol. 14, no. 2, pp. 2417-2430, Feb. 2014.

[17] N. Marsi, B. Y. Majlis, A. A. Hamzah, and F. Mohd-Yasin, "A MEMS packaged capacitive pressure sensor employing 3C-SiC with operating temperature of 500° C," *Microsyst. Technol.,* vol. 21, no. 1, pp. 9-20, Jan. 2015.

[18] J. Konstantinova, A. Stilli, and K. Althoefer, "Fingertip fiber optical tactile array with two-level spring structure," *Sensors,* vol. 17, no. 10, p. 2337, Oct. 2017.

[19] K. Shimonomura, "Tactile image sensors employing camera: A review," *Sensors,* vol. 19, no. 18, p. 3933, Jan. 2019.

[20] L. Pan *et al.*, "An ultra-sensitive resistive pressure sensor based on hollow-sphere microstructure induced elasticity in conducting polymer film," *Nat. Commun.,* vol. 5, no. 1, pp. 1-8, Jan. 2014.

[21] X. Sun, C. Wang, C. Chi, N. Xue, and C. Liu, "A highly-sensitive flexible tactile sensor array utilizing piezoresistive carbon nanotube–polydimethylsiloxane composite," *J. Micromech. Microeng.,* vol. 28, no. 10, p. 105011, July 2018.

[22] M. Gála, J. Barabáš, and M. Kopásková, "User presence monitoring based on Velostat pressure sensors and Arduino platform," *2020 IEEE 21st Int. Conf. Comput. Probl. Electr. Eng. (CPEE)*, 2020, pp. 1-3.

[23] A. Fatema, S. Poondla, R. B. Mishra and A. M. Hussain, "A Low-Cost Pressure Sensor Matrix for Activity Monitoring in Stroke Patients Using Artificial Intelligence," *IEEE Sens. J.*, vol. 21, no. 7, pp. 9546-9552, Apr. 2021.

[24] S. Sundaram, P. Kellnhofer, Y. Li, J.-Y. Zhu, A. Torralba, and W. Matusik, "Learning the signatures of the human grasp using a scalable tactile glove," *Nature,* vol. 569, no. 7758, pp. 698-702, May 2019.

[25] D. Chen, Y. Cai, and M.-C. Huang, "Customizable pressure sensor array: Design and evaluation," *IEEE Sens. J.,* vol. 18, no. 15, pp. 6337-6344, May 2018.

[26] D. Chen *et al.*, "Smart insole-based indoor localization system for Internet of Things applications," *IEEE Internet Things J.,* vol. 6, no. 4, pp. 7253-7265, May 2019.

[27] R. Hudec, S. Matúška, P. Kamencay, and M. Benco, "A Smart IoT System for Detecting the Position of a Lying Person Using a Novel Textile Pressure Sensor," *Sensors,* vol. 21, no. 1, p. 206, Jan. 2021.

[28] M. Hopkins, R. Vaidyanathan, and A. H. Mcgregor, "Examination of the performance characteristics of velostat as an in-socket pressure sensor," *IEEE Sens. J.,* vol. 20, no. 13, pp. 6992-7000, Mar. 2020.

[29] J. Niu, C. Zhang, X. Chen, C. Ma, L. Chen, and C. Tong, "A novel helmet fitness evaluation device based on the flexible pressure sensor matrix," *Sensors,* vol. 19, no. 18, p. 3823, Jan. 2019.

[30] Z. Del Prete, L. Monteleone, and R. Steindler, "A novel pressure array sensor based on contact resistance variation: Metrological properties," *Rev. Sci. Instrum.,* vol. 72, no. 2, pp. 1548-1553, Feb. 2001.

[31] J. A. Hidalgo-López, Ó. Oballe-Peinado, J. Castellanos-Ramos, J. A. Sánchez-Durán, R. Fernández-Ramos, and F. Vidal-Verdú, "High-accuracy readout electronics for piezoresistive tactile sensors," *Sensors,* vol. 17, no. 11, p. 2513, Nov. 2017.

[32] J. M. Gandarias, A. J. Garcia-Cerezo, and J. M. Gomez-de-Gabriel, "CNN-based methods for object recognition with high-resolution tactile sensors," *IEEE Sens. J.,* vol. 19, no. 16, pp. 6872-6882, Apr. 2019.

[33] W. Min, H. Cui, Q. Han, and F. Zou, "A scene recognition and semantic analysis approach to unhealthy sitting posture detection during screen-reading," *Sensors,* vol. 18, no. 9, p. 3119, Sep. 2018.

[34] M.-O. Park and S.-H. Lee, "Effects of seating education and cushion management for adaptive sitting posture in spinal cord injury: Two case reports," *Medicine,* vol. 98, no. 4, Jan. 2019.

[35] C. Ma, W. Li, R. Gravina, J. Du, Q. Li, and G. Fortino, "Smart Cushion-Based Activity Recognition: Prompting Users to Maintain a Healthy Seated Posture," *IEEE Trans. Syst. Man Cybern. Syst.,* vol. 6, no. 4, pp. 6-14, Oct. 2020.

[36] L. Feng, Z. Li, and C. Liu, "Are you sitting right?-sitting posture recognition using RF signals," *2019 IEEE Pac. Rim Conf. Commun. Comp. Signal Process. (PACRIM)*, 2019, pp. 1-6.

[37] M. Ding, T. Suzuki, and T. Ogasawara, "Estimation of driver's posture using pressure distribution sensors in driving simulator and on-road experiment," *2017 IEEE Int. Conf. Cyborg Bionic Syst. (CBS)*, 2017, pp. 215-220.

[38] O. Halabi, S. Fawal, E. Almughani, and L. Al-Homsi, "Driver activity recognition in virtual reality driving simulation," *2017 8th Int. Conf. Inf. Commun. Syst. (ICICS)*, 2017, pp. 111-115.

[39] M. Khalil, N. Power, E. Graham, S.S. Deschênes, N. Schmitz, "The association between sleep and diabetes outcomes—A systematic review," *Diabetes Res. Clin. Pract.* vol. 161, p. 108035, Mar. 2020.

[40] J.-H. Park, C. Yoo, E. Yoo, and Y. Y. Kim, "Intraocular pressure elevation during lateral body posture in side-sleeping glaucoma patients," *Optom. Vis. Sci.*, vol. 96, no. 1, pp. 62-70, Jan. 2019.

[41] T.-E. Lee, C. Yoo, and Y. Y. Kim, "Effects of different sleeping postures on intraocular pressure and ocular perfusion pressure in healthy young subjects," *Ophthalmology*, vol. 120, no. 8, pp. 1565-1570, Aug. 2013.

[42] J. C. T. Mallare *et al.*, "Sitting posture assessment using computer vision," *2017 IEEE 9th Int. Conf. Hum. Nanotechnol. Inf. Technol. Commun. Control Environ. Manage. (HNICEM)*, 2017, pp. 1-5.

[43] A. Y.-C. Tam, B. P.-H. So, T. T.-C. Chan, A. K.-Y. Cheung, D. W.-C. Wong, and J. C.-W. Cheung, "A Blanket Accommodative Sleep Posture Classification System Using an Infrared Depth Camera: A Deep Learning Approach with Synthetic Augmentation of Blanket Conditions," *Sensors*, vol. 21, no. 16, p. 5553, Jan. 2021.

[44] A. Petropoulos, D. Sikeridis, and T. Antonakopoulos, "SPoMo: IMU-based real-time sitting posture monitoring," *2017 IEEE 7th Int. Conf. Consum. Electron.-Berlin (ICCE-Berlin)*, 2017, pp. 5-9.

[45] R. M. Kwasnicki et al., "A lightweight sensing platform for monitoring sleep quality and posture: a simulated validation study," *Eur. J. Med. Res.*, vol. 23, no. 1, pp. 1-9, Dec. 2018.

[46] C. Ma, W. Li, R. Gravina, and G. Fortino, "Posture detection based on smart cushion for wheelchair users," *Sensors,* vol. 17, no. 4, p. 719, Apr. 2017.

[47] Z. A. Abro et al., "Development of FBG pressure sensors using FDM technique for monitoring sleeping postures," *Sens. Actuator A Phys.*, p. 112921, Jun. 2021

[48] E. Fragkiadakis, K. V. Dalakleidi, and K. S. Nikita, "Design and Development of a Sitting Posture Recognition System," *2019 41st Conf. Proc. IEEE. Eng. Med. Biol. Soc. (EMBC)*, 2019, pp. 3364-3367.

[49] Y. Zhu *et al.*, "A Smart Portable Mat That Can Meausre Sitting Plantar Pressure Distribution with a High Resolution," *2019 IEEE 6th Int. Conf. Ind. Eng. Appl. (ICIEA)*, 2019, pp. 141-144.

[50] H. Ai, L. Zhang, Z. Yuan, and H. Huang, "iCushion: A Pressure Map Algorithm for High Accuracy Human Identification," *2018 24th Int. Conf. Pattern Recognit. (ICPR)*, 2018, pp. 3483-3488.

[51] S. Hongchang, Z. Zhijing, J. Xin, D. Sanpeng, J. Yongxiang, and Z. Zhongpeng, "Monitoring driving psychological fatigue through unconstrained heartbeat signal extraction by using pressure sensor array," *IEEE Access,* vol. 8, pp. 22193-22202, Dec. 2019.

[52] J. Wang, B. Hafidh, H. Dong, and A. El Saddik, "Sitting Posture Recognition Using a Spiking Neural Network," *IEEE Sens. J.,* vol. 21, no. 2, pp. 1779-1786, Aug. 2020.

[53] N. Carbonaro, M. Laurino, L. Arcarisi, D. Menicucci, A. Gemignani, and A. Tognetti, "Textile-Based Pressure Sensing Matrix for In-Bed Monitoring of Subject Sleeping Posture and Breathing Activity," *Appl. Sci.*, vol. 11, no. 6, p. 2552, Jan. 2021.

[54] Q. Hu, X. Tang and W. Tang, "A Real-Time Patient-Specific Sleeping Posture Recognition System Using Pressure Sensitive Conductive Sheet and Transfer Learning," *IEEE Sens. J.*, vol. 21, no. 5, pp. 6869-6879, Mar. 2021.

[55] I. Vehec and L. Livovsky, "Flexible Resistive Sensor Based on Velostat," *2020 43rd Int. Spring Semin. Electron. Technol. (ISSE)*, 2020, pp. 1-6.

[56] A. Dzedzickis *et al.*, "Polyethylene-Carbon Composite (Velostat®) Based Tactile Sensor," *Polymers,* vol. 12, no. 12, p. 2905, Dec. 2020.

[57] M. J. Edmonds, "Learning Complex Functional Manipulations by Human Demonstration and Fluent Discovery," M.S. thesis, Dept. of Comp. Sci., UCLA, Los Angeles, CA, 2017.

[58] S. Chen, M. Li, Y. Huang, H. Xu, G. Gu, and X. Guo, "Matrix-Addressed Flexible Capacitive Pressure Sensor With Suppressed Crosstalk for Artificial Electronic Skin," *IEEE Trans. Electron. Devices,* vol. 67, no. 7, pp. 2940-2944, May 2020.

[59] A. Tihak and D. Bošković, "Experimental evaluation of challenges in designing a resistive pressure sensors," *IEEE EUROCON 2019-18th Int. Conf. Smart Technol.*, July 2019, pp. 1-6.

[60] F. Castro, T. Pentiado, J. Blanco, R. Xavier, M. Sanches and A. de Carvalho, "Crosstalk Error Analysis in IIDFC Readout Circuit for Use in Piezoresistive Composite," *IEEE Sens. J.*, vol. 18, no. 1, pp. 382-389, Jan. 2018.

[61] B. Fan, S. Chen, J. Gao, and X. Guo, "Accurate Recognition of Lightweight Objects With Low Resolution Pressure Sensor Array," *IEEE Sens. J.,* vol. 20, no. 6, pp. 3280-3284, Dec. 2019.

[62] C. Medrano-Sánchez, R. Igual-Catalán, V. H. Rodríguez-Ontiveros, and I. Plaza-García, "Circuit analysis of matrix-like resistor networks for eliminating crosstalk in pressure sensitive mats," *IEEE Sens. J.,* vol. 19, no. 18, pp. 8027-8036, May 2019.

[63] J.-F. Wu, "Scanning approaches of 2-D resistive sensor arrays: A review," *IEEE Sens. J.,* vol. 17, no. 4, pp. 914-925, Dec. 2016.

[64] L. Shu, X. Tao, and D. D. Feng, "A new approach for readout of resistive sensor arrays for wearable electronic applications," *IEEE Sens. J.,* vol. 15, no. 1, pp. 442-452, June 2014.

[65] S. Suprapto, A. Setiawan, H. Zakaria, W. Adiprawita, and B. Supartono, "Low-cost pressure sensor matrix using velostat," *2017 5th Int. Conf. Instrum. Commun. Inf. Technol. Biomed. Eng. (ICICI-BME)*, 2017, pp. 137-140.

[66] S. Koh, B. Cho, J.-K. Park, C.-H. Kim, and S. Lee, "A Fundamental Experiment on Contact Position Estimation on Vision based Dome-type Soft Tactile Sensor using Ready-made Medium," *2019 13th Int. Conf. Sens. Technol. (ICST)*, 2019, pp. 1-5.

[67] V. Chhoeum, Y. Kim and S. D. Min, "A Convolution Neural Network Approach to Access Knee Joint Angle Using Foot Pressure Mapping Images: A Preliminary Investigation," *IEEE Sens. J.*, vol. 21, no. 15, pp. 16937-16944, Aug. 2021.

[68] O. Ozioko, W. T. Navaraj, N. Yogeswaran, M. Hersh, and R. Dahiya, "Tactile Communication system for the Interaction between Deafblind and Robots," *2018 27th IEEE Int. Symp. Robot Hum. Interact. Commun. (RO-MAN)*, 2018, pp. 416-421.

[69] J. M. Gandarias, J. M. Gómez-de-Gabriel, and A. J. García-Cerezo, "Enhancing perception with tactile object recognition in adaptive grippers for human–robot interaction," *Sensors*, vol. 18, no. 3, p. 692, Mar. 2018.

[70] Q. Wan, H. Zhao, J. Li, and P. Xu, "Hip Positioning and Sitting Posture Recognition Based on Human Sitting Pressure Image," *Sensors*, vol. 21, no. 2, p. 426, Jan. 2021.

[71] S. Stassi, V. Cauda, G. Canavese, and C. F. Pirri, "Flexible tactile sensing based on piezoresistive composites: A review," *Sensors,* vol. 14, no. 3, pp. 5296-5332, Mar. 2014.

[72] X.-W. Zhang, Y. Pan, Q. Zheng, and X.-S. Yi, "Time dependence of piezoresistance for the conductor-filled polymer composites," *J. Polym. Sci. B Polym. Phys.,* vol. 38, no. 21, pp. 2739-2749, Nov. 2000.

[73] X. Zhang and X. Ye, "Zero potential method measurement error analysis for networked resistive sensor arrays," *IET Sci. Meas. Technol.,* vol. 11, no. 3, pp. 235-240, May 2016.

[74] A. Krizhevsky, I. Sutskever, and G. E. Hinton, "Imagenet classification with deep convolutional neural networks," *Adv. Neural Inf. Process. Syst.*, vol. 25, pp. 1097-1105, 2012.

[75] K. Simonyan and A. Zisserman, "Very deep convolutional networks forlarge-scale image recognition," *arXiv preprint arXiv:1409.1556*, 2014.

[76] K. He, X. Zhang, S. Ren, and J. Sun, "Deep residual learning for image recognition," *2016 IEEE Conf. Comput. Vis. Pattern Recognit. (CVPR)*, 2016, pp. 770-778.

[77] A. Drimus, G. Kootstra, A. Bilberg, and D. Kragic, "Design of a flexible tactile sensor for classification of rigid and deformable objects," *Robot. Auton. Syst.*, vol. 62, no. 1, pp. 3-15, Jan. 2014.

[78] A. Shibata, A. Ikegami, M. Nakauma, and M. Higashimori, "Convolutional neural network based estimation of gel-like food texture by a robotic sensing system," *Robotics*, vol. 6, no. 4, p. 37, Dec. 2017.

[79] F. Pastor, J. M. Gandarias, A. J. García-Cerezo, and J. M. Gómez-de-Gabriel, "Using 3d convolutional neural networks for tactile object recognition with robotic palpation," *Sensors*, vol. 19, no. 24, p. 5356, Jan. 2019.

[80] F. Baghaei Naeini *et al.*, "A Novel Dynamic-Vision-Based Approach for Tactile Sensing Applications," *IEEE Trans. Instrum. Meas.*, vol. 69, no. 5, pp. 1881-1893, May 2020.

[81] Z. Deng, Y. Jonetzko, L. Zhang, and J. Zhang, "Grasping force control of multi-fingered robotic hands through tactile sensing for object stabilization," *Sensors*, vol. 20, no. 4, p. 1050, Feb. 2020.

[82] C. Ledig et al., "Photo-Realistic Single Image Super-Resolution Using a Generative Adversarial Network," *2017 IEEE Conf. Comput. Vis. Pattern Recognit. (CVPR)*, 2017, pp. 105-114.

[83] S. Liu, X. Huang, N. Fu, C. Li, Z. Su, and S. Ostadabbas, "Simultaneously-collected multimodal lying pose dataset: Towards in-bed human pose monitoring under adverse vision conditions," *arXiv preprint arXiv:2008.08735,* Aug. 2020.